

Supplementary note on diffractive analyses of 2015 proton-proton data:

- [1] Measurement of Central Exclusive Production of $h\bar{h}$ pairs $(h=\pi,K,p)$ with Roman Pot detectors in diffractive proton-proton interactions at $\sqrt{s}=200~{\rm GeV}$
- [2] Measurement of particle production with Roman Pot detectors in diffractive proton-proton interactions at $\sqrt{s} = 200 \text{ GeV}$

Leszek Adamczyk¹, Łukasz Fulek¹, and Rafał Sikora¹

¹AGH University of Science and Technology, FPACS, Kraków, Poland

May 15, 2018

Abstract

In this note we present supplementary material related to analyses of diffractive processes based on 2015 data from proton-proton collisions at $\sqrt{s}=200$ GeV. This dataset was collected with newly installed Roman Pot detectors in Phase II* configuration which ensured efficient triggering and measuring diffractively scattered protons.

We focus on calculation of efficiencies, corrections to Monte Carlo simulations and derivation of systematic uncertainties of our measurements.

Contents

1	Efficiencies	3
	1.1 TPC track acceptance and reconstruction efficiency	3
	1.2 TOF acceptance, hit reconstruction and track-matching efficiency	16
	1.3 TPC vertex reconstruction efficiency	29
2	Roman Pot simulation	30
3	$\mathrm{d}E/\mathrm{d}x$ correction	31
4	TPC track pointing resolution adjustment	35
5	Dead material in front of TPC	38
6	Systematic errors	39
Li	ist of Figures	40
Li	ist of Tables	40
\mathbf{R}	eferences	41

1. Efficiencies

1.1 TPC track acceptance and reconstruction efficiency

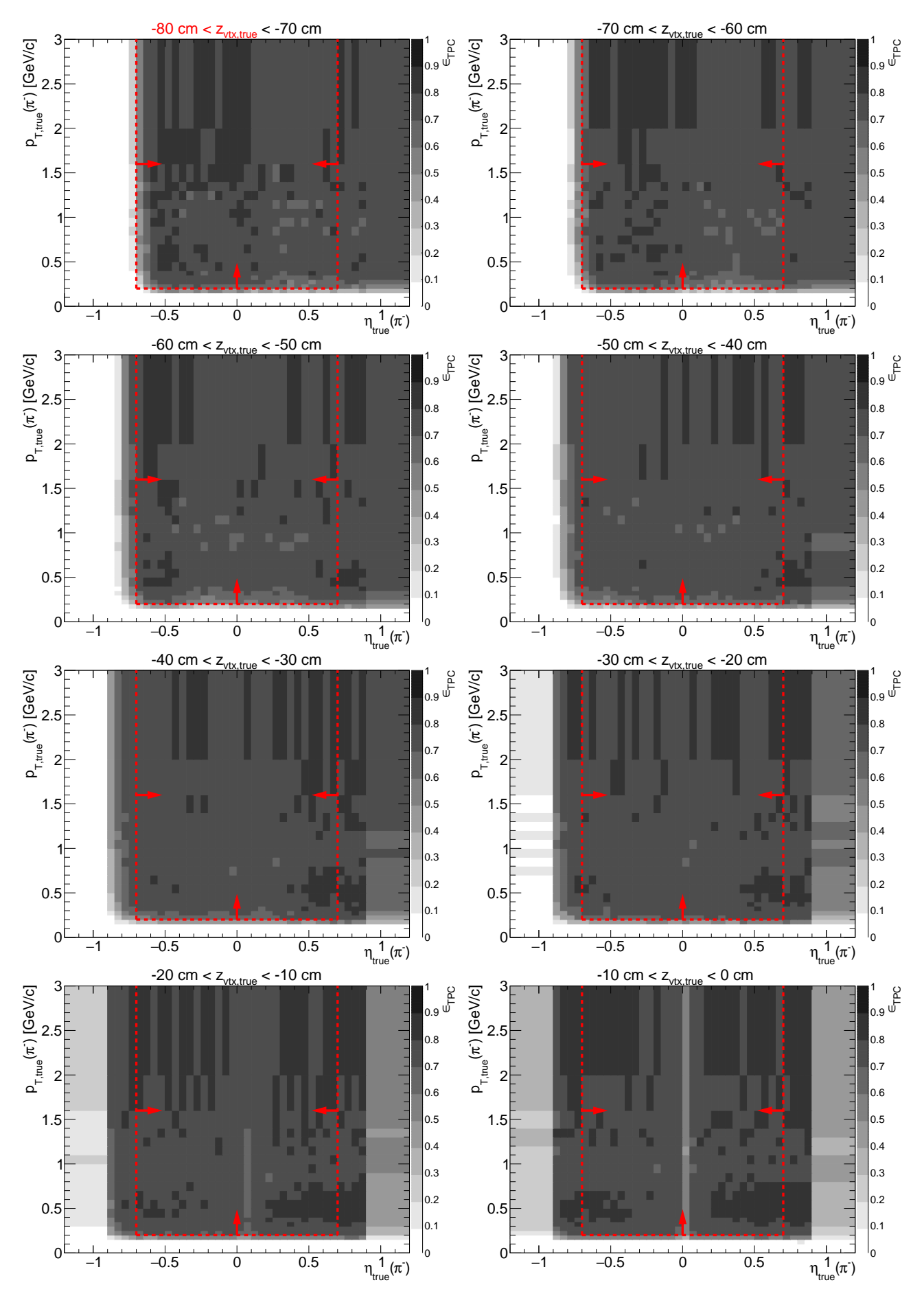
We define joint acceptance and efficiency of the reconstruction of a track in the TPC, ϵ_{TPC} , as the probability that particle from the primary interaction generates signal in the detector which is reconstructed as a track that satisfies all quality criteria and whose p_T and η are within the kinematic region of the measurement (cuts ?? and ??).

The chnically this quantity is derived from STARsim MC embedded into zero-bias triggers in the following procedure:

- 1. True-level primary particles of given ID and charge, with all physics $(p_T^{\text{true}}, \eta^{\text{true}})$ and detector (z_{vx}) quantities within defined region of the measurement, are selected (set A).
- 2. Each particle from set A is checked if global TPC track with more than half of hit points generated by this particle, was reconstructed. All global tracks which are associated with true-level primary particles and satisfy kinematic and quality criteria (cuts ?? and ??), form set B.
- 3. The joint TPC acceptance and efficiency is calculated as the ratio of the histograms of true-level quantities (such as p_T , η , z_{vx}) for particles from set B and particles from set A:

$$\epsilon_{\text{TPC}}(p_T, \eta, z_{vx}; \text{ sign, PID}) = \frac{(p_T, \eta, z_{vx}) \text{ histogram for particles of given sign and ID from } set B}{(p_T, \eta, z_{vx}) \text{ histogram for particles of given sign and ID from } set A}. (1.1)$$

Figure 1.1: TPC acceptance and reconstruction efficiency of π^- . Each plot represents the TPC efficiency ϵ_{TPC} (z-axis) as a function of true particle pseudorapidity η (x-axis) and transverse momentum p_T (y-axis) in single z-vertex bin whose range is given at the top. Red lines and arrows indicate region accepted in analyses.



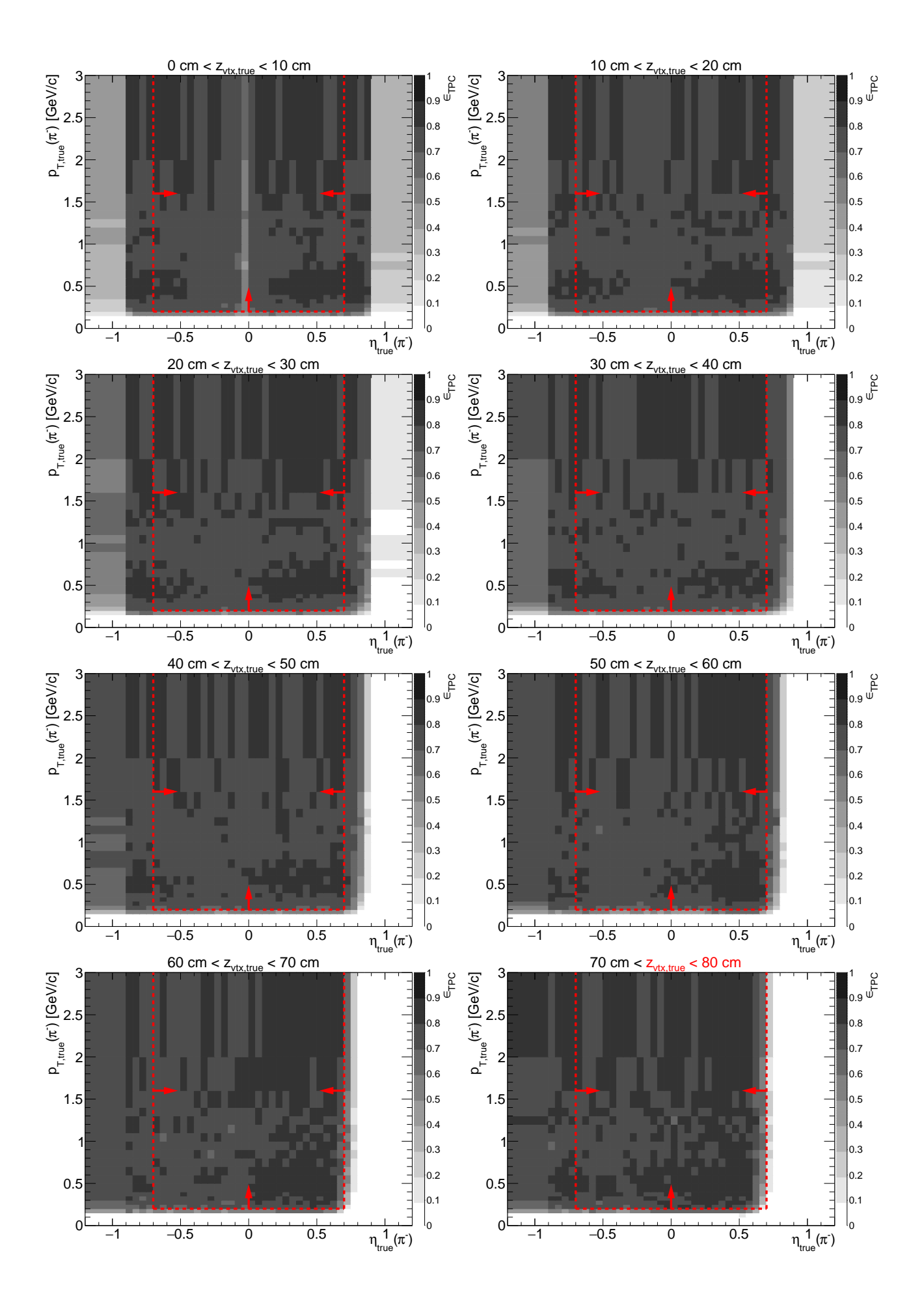
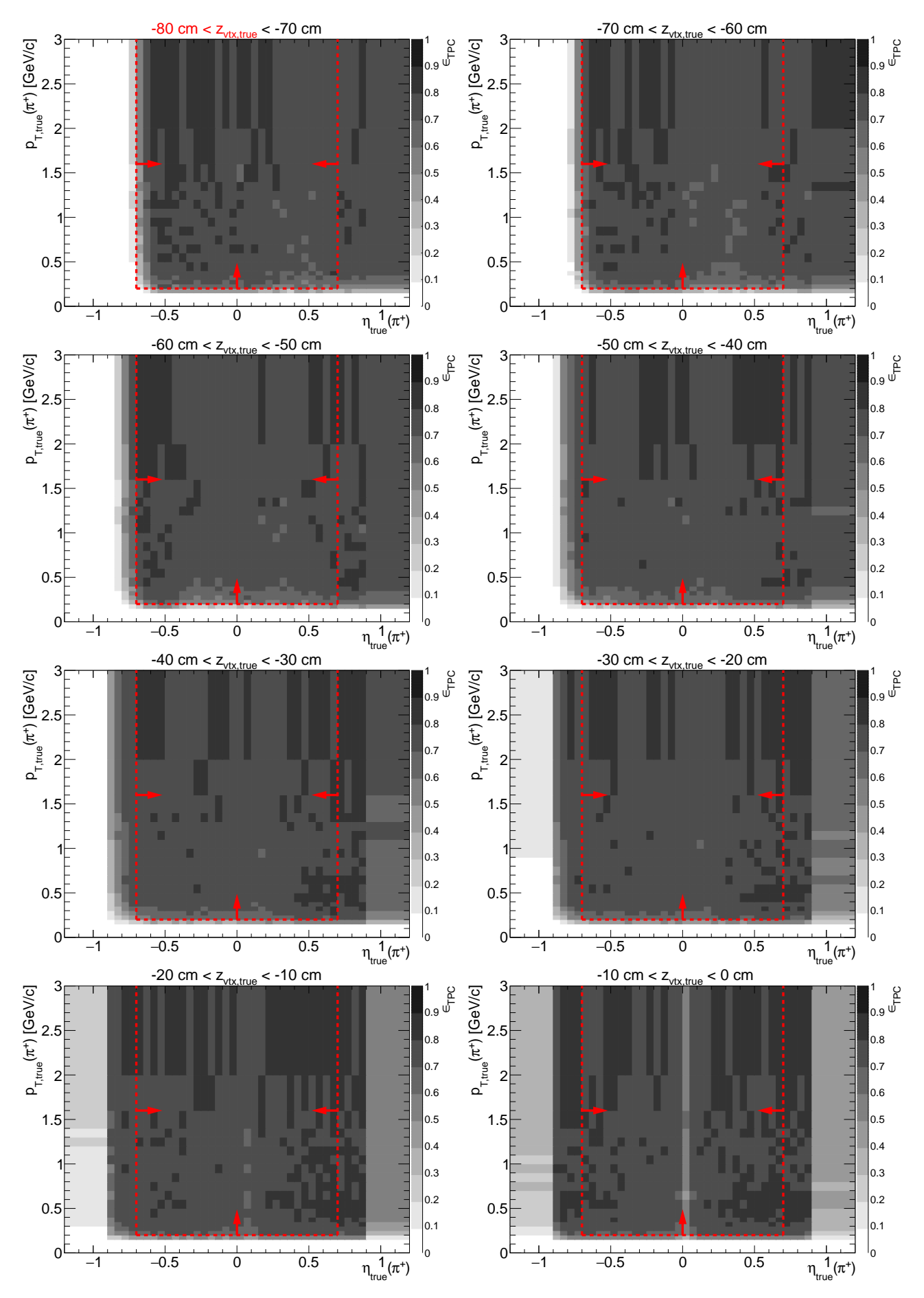


Figure 1.2: TPC acceptance and reconstruction efficiency of π^+ . Each plot represents the TPC efficiency ϵ_{TPC} (z-axis) as a function of true particle pseudorapidity η (x-axis) and transverse momentum p_T (y-axis) in single z-vertex bin whose range is given at the top. Red lines and arrows indicate region accepted in analyses.



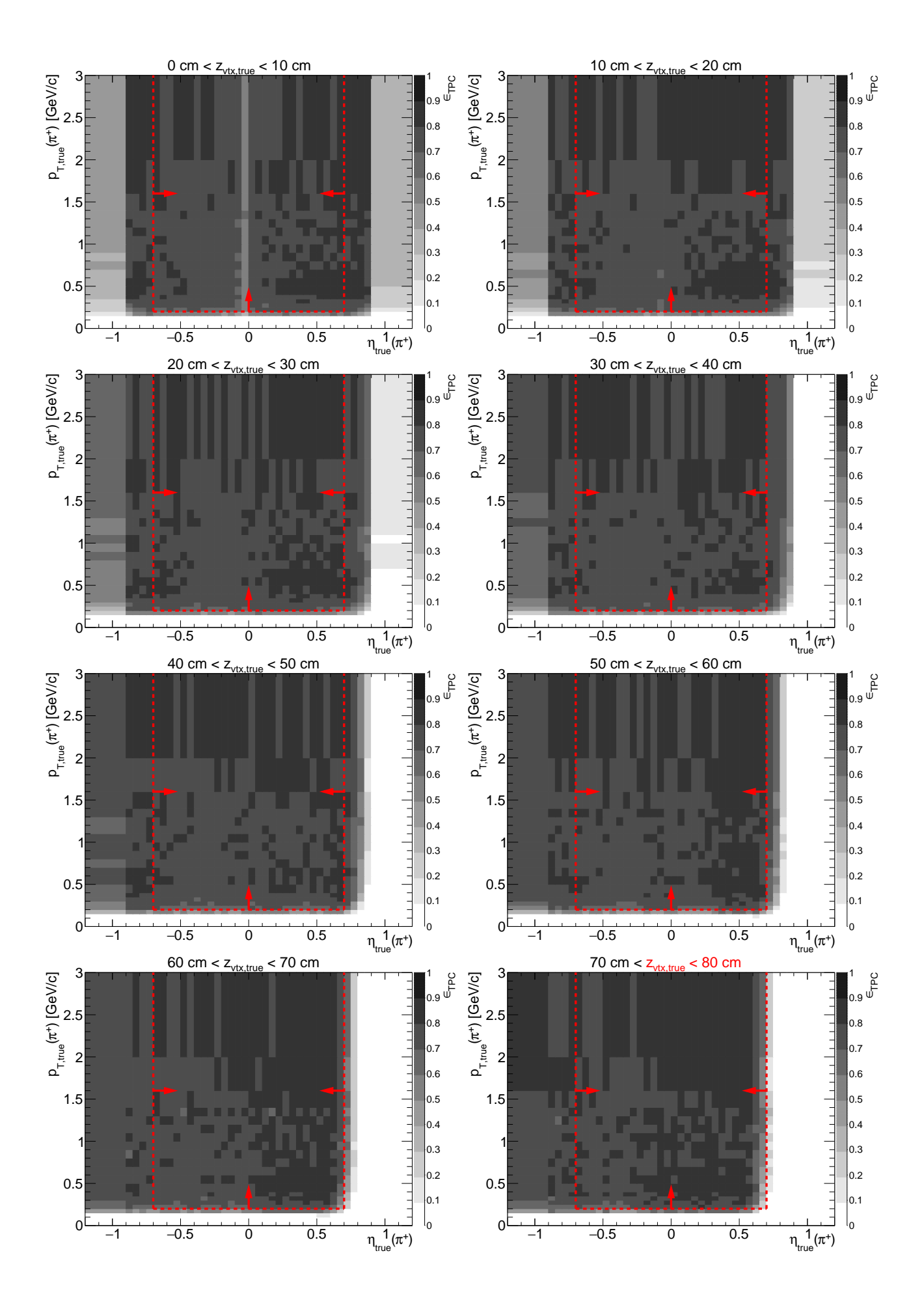
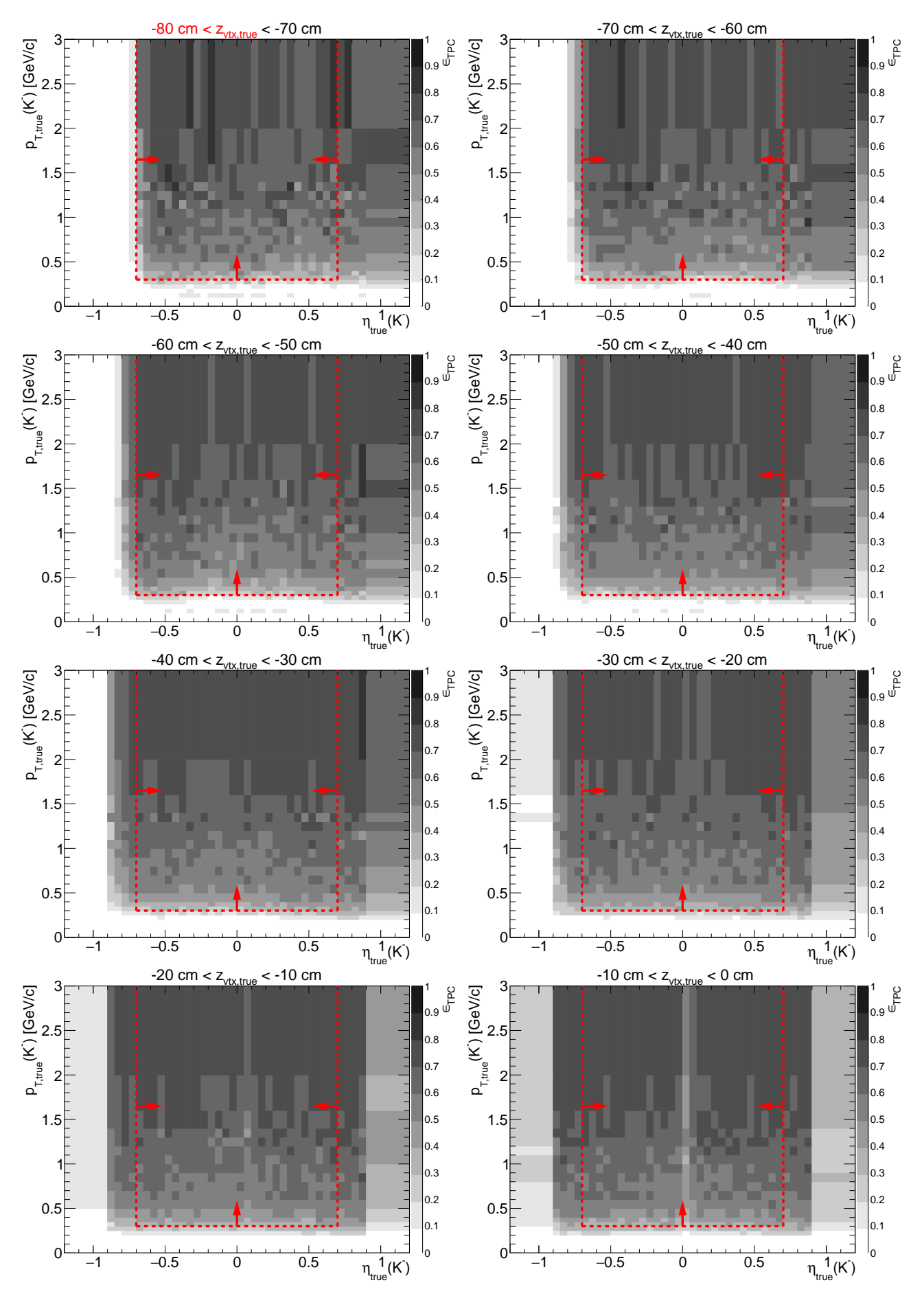


Figure 1.3: TPC acceptance and reconstruction efficiency of K^- . Each plot represents the TPC efficiency ϵ_{TPC} (z-axis) as a function of true particle pseudorapidity η (x-axis) and transverse momentum p_T (y-axis) in single z-vertex bin whose range is given at the top. Red lines and arrows indicate region accepted in analyses.



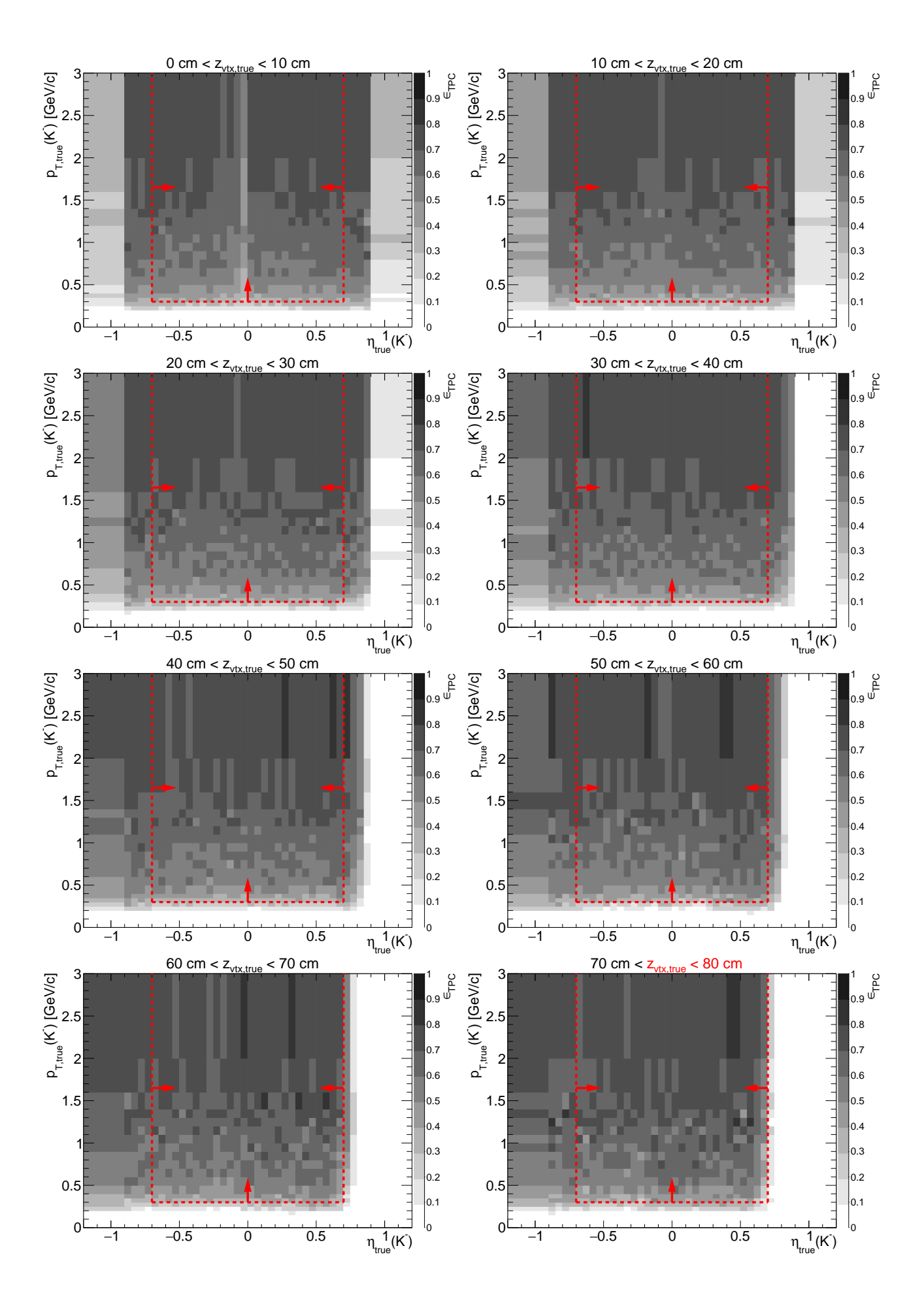
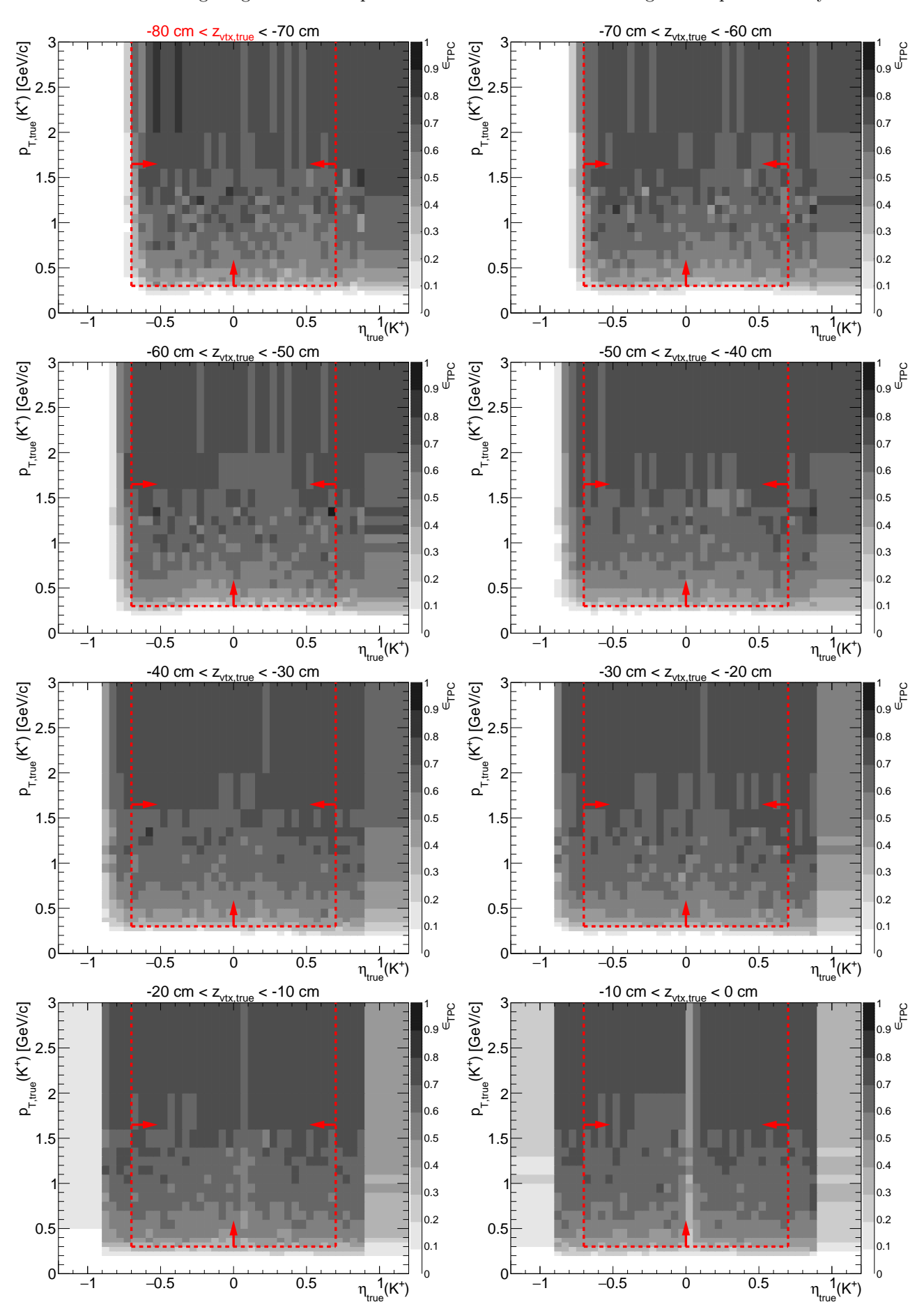


Figure 1.4: TPC acceptance and reconstruction efficiency of K^+ . Each plot represents the TPC efficiency ϵ_{TPC} (z-axis) as a function of true particle pseudorapidity η (x-axis) and transverse momentum p_T (y-axis) in single z-vertex bin whose range is given at the top. Red lines and arrows indicate region accepted in analyses.



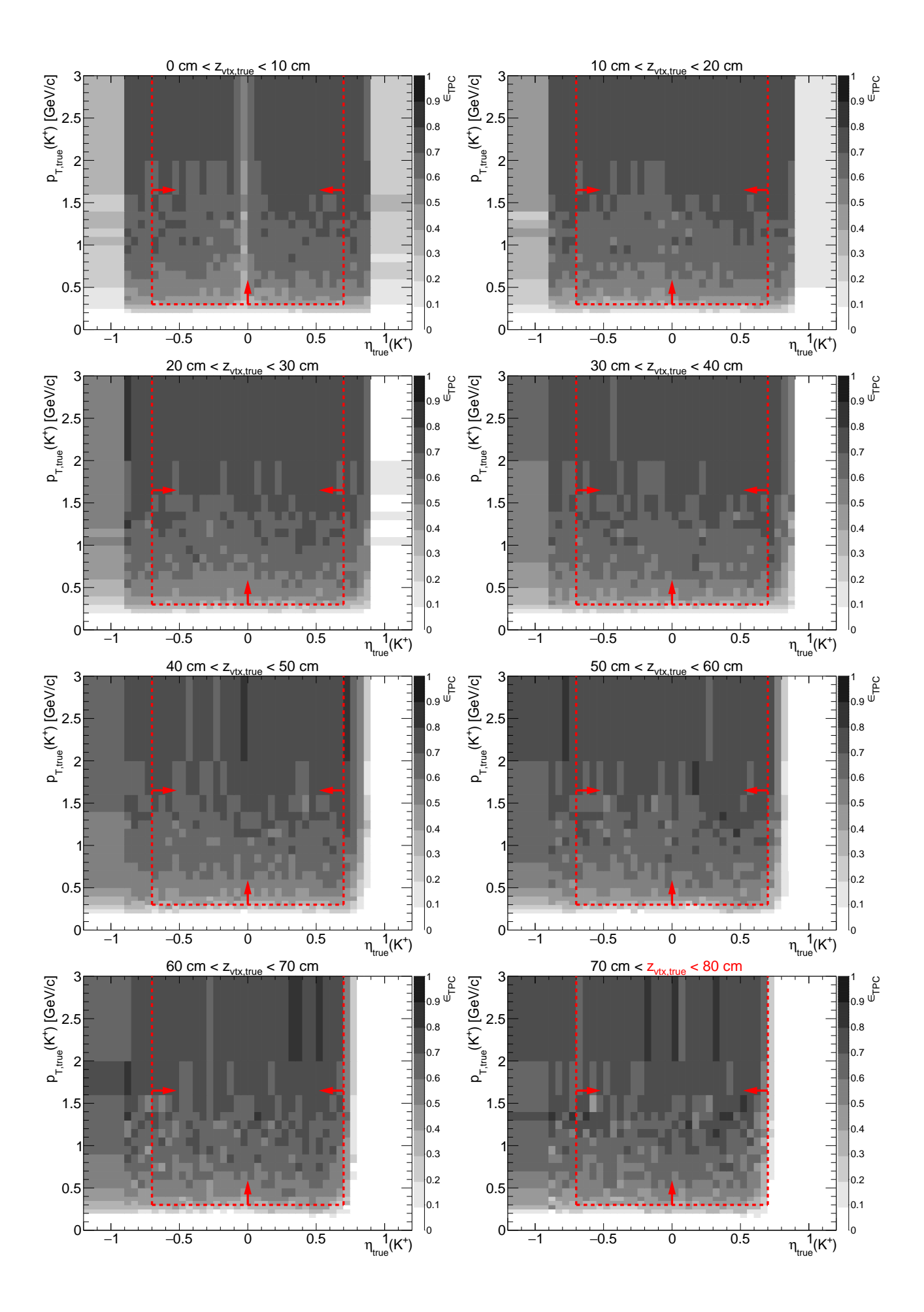
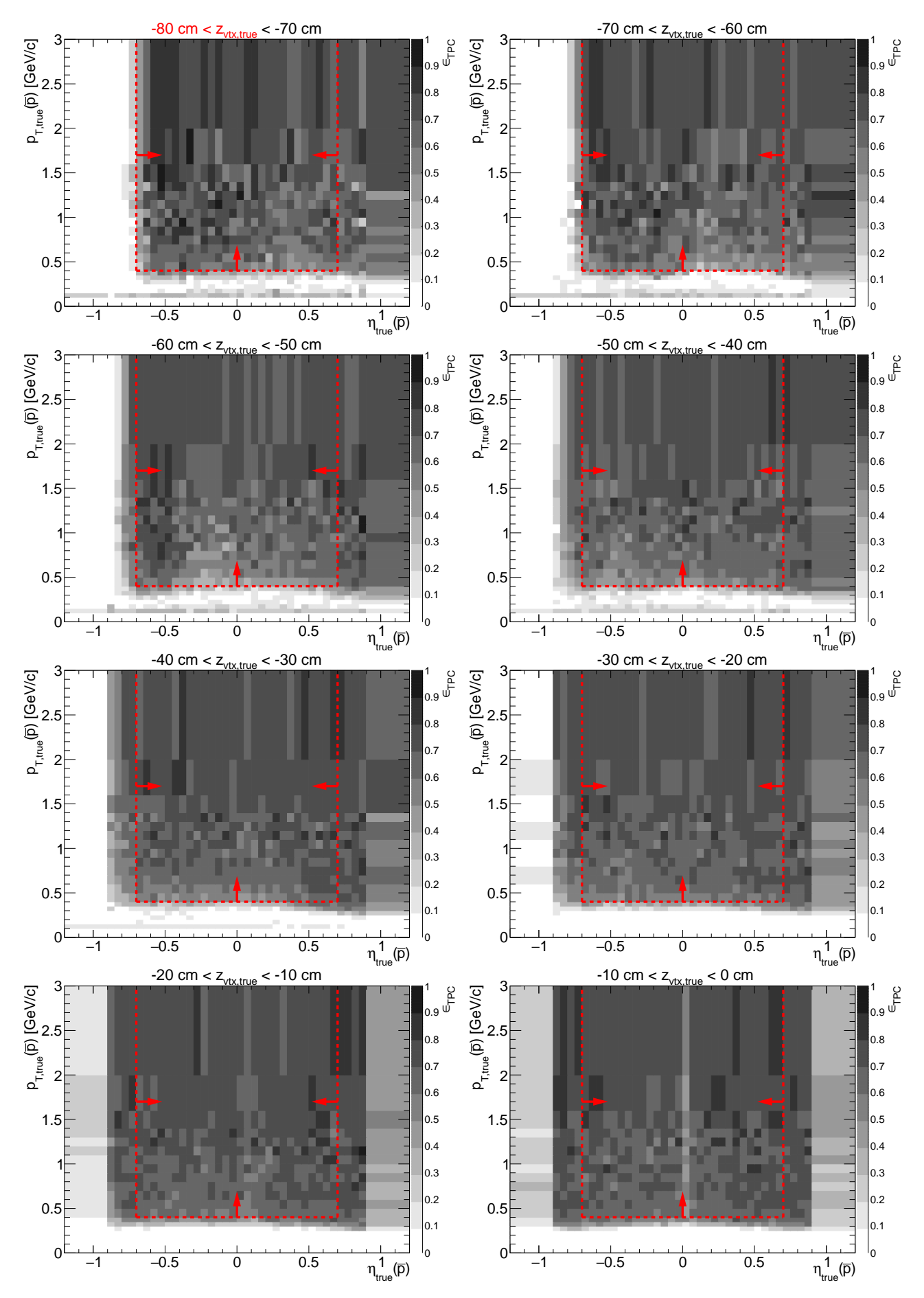


Figure 1.5: TPC acceptance and reconstruction efficiency of \bar{p} . Each plot represents the TPC efficiency ϵ_{TPC} (z-axis) as a function of true particle pseudorapidity η (x-axis) and transverse momentum p_T (y-axis) in single z-vertex bin whose range is given at the top. Red lines and arrows indicate region accepted in analyses.



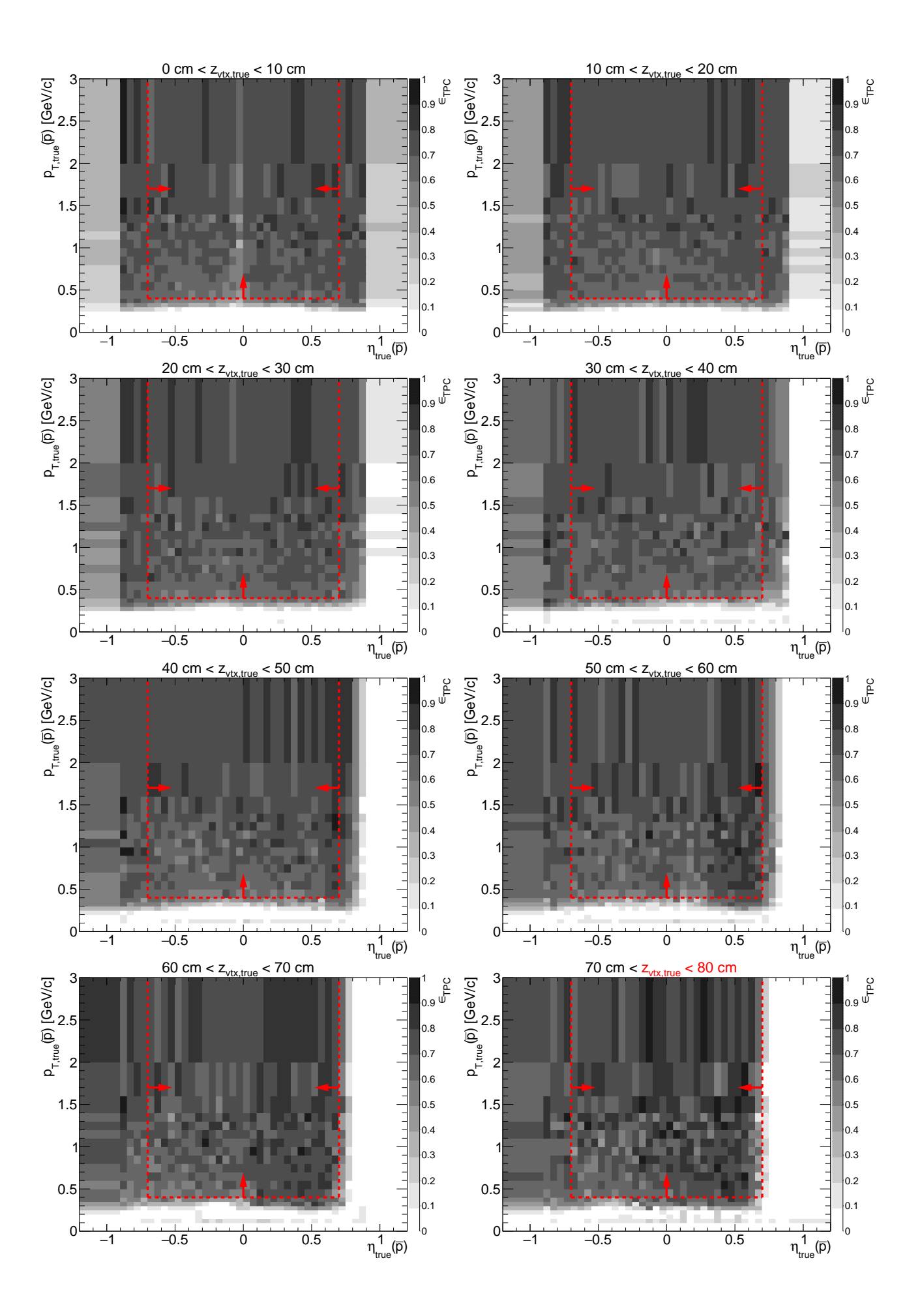
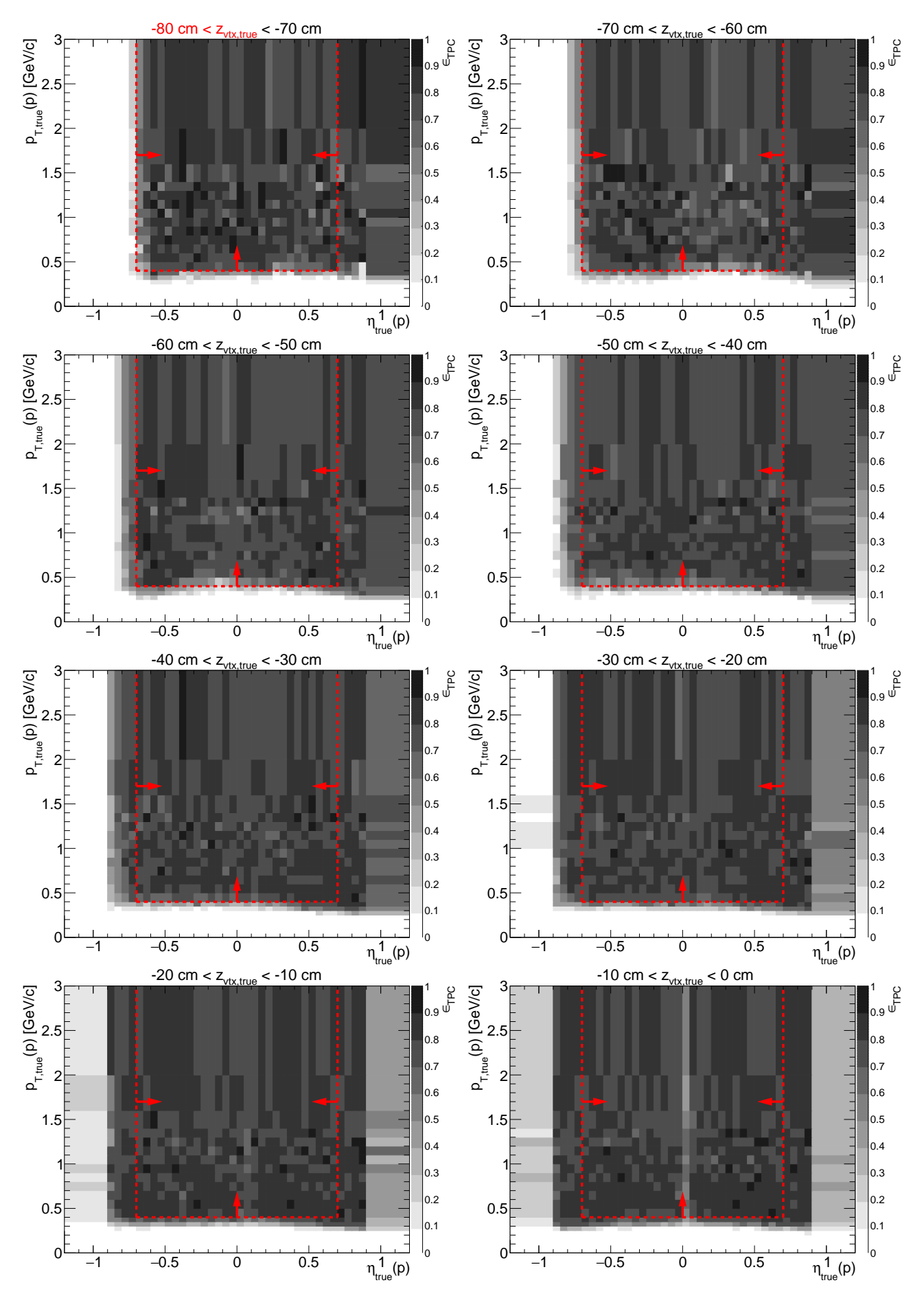
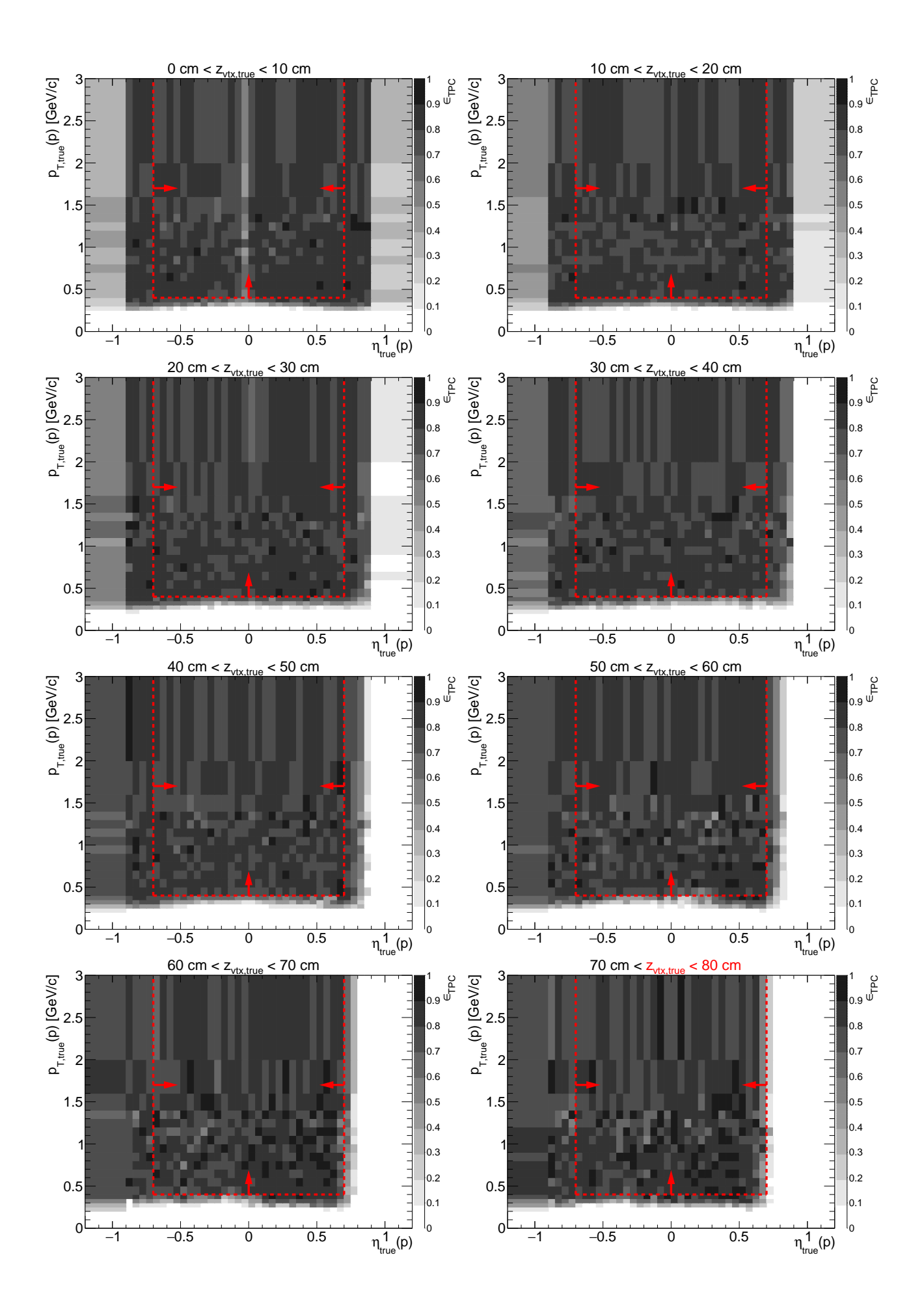


Figure 1.6: TPC acceptance and reconstruction efficiency of p. Each plot represents the TPC efficiency ϵ_{TPC} (z-axis) as a function of true particle pseudorapidity η (x-axis) and transverse momentum p_T (y-axis) in single z-vertex bin whose range is given at the top. Red lines and arrows indicate region accepted in analyses.





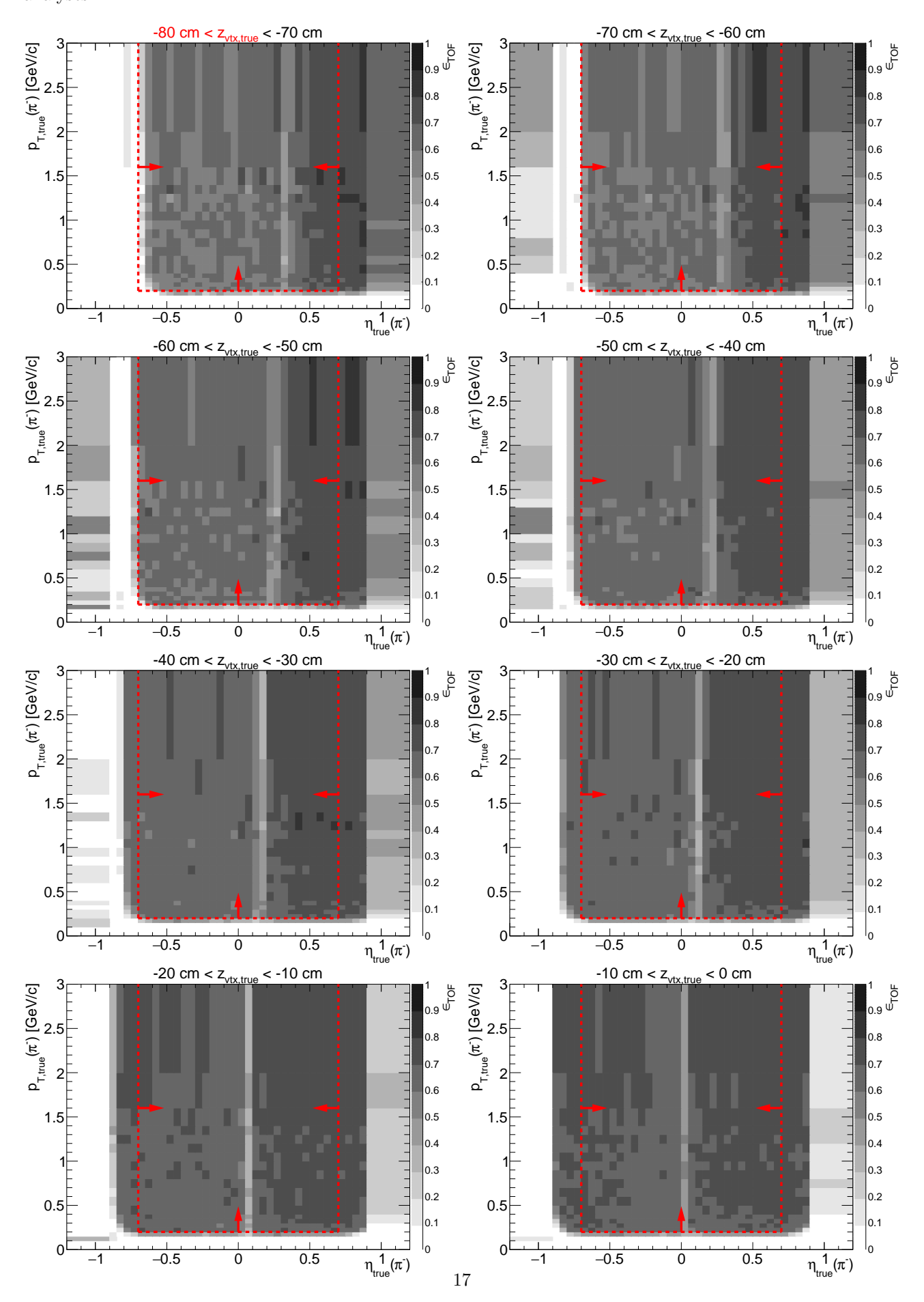
1.2 TOF acceptance, hit reconstruction and track-matching efficiency

Combined TOF acceptance, hit reconstruction efficiency and matching efficiency with TPC tracks, ϵ_{TOF} , is defined as the probability that the global TPC track that satisfy kinematic and quality criteria (cuts ?? and ??) is matched with hit in TOF (matching flag of the track is different from 0). This quantity is generally referred as "TOF efficiency".

It is calculated in two ways. In the first approach the STARsim MC embedded into zero-bias triggers is used. Tracks belonging to $set\ B$ from Sec. ?? are utilized. From these tracks a sub-sample of tracks with non-zero TOF matching flag is extracted ($set\ C$). The TOF efficiency is calculated as

$$\epsilon_{\text{\tiny TOF}}\left(p_T, \eta, z_{vx}; \text{ sign}, \text{PID}\right) = \frac{(p_T, \eta, z_{vx}) \text{ histogram for particles of given sign and ID from } set \ C}{(p_T, \eta, z_{vx}) \text{ histogram for particles of given sign and ID from } set \ B}. \tag{1.2}$$

Figure 1.7: TOF acceptance, reconstruction and matching efficiency of π^- . Each plot represents the TOF efficiency ϵ_{TOF} (z-axis) as a function of true particle pseudorapidity η (x-axis) and transverse momentum p_T (y-axis) in single z-vertex bin whose range is given at the top. Red lines and arrows indicate region accepted in analyses.



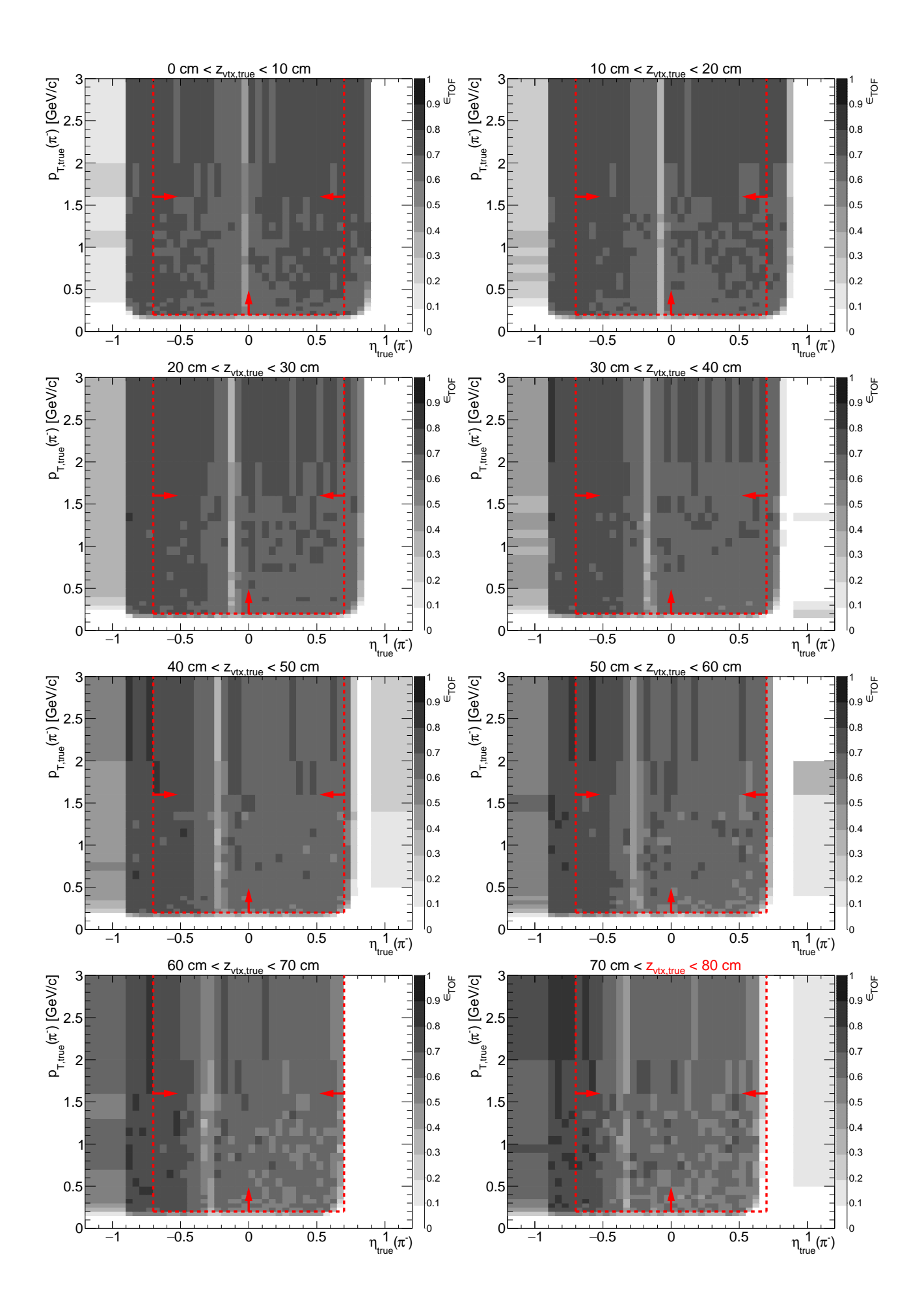
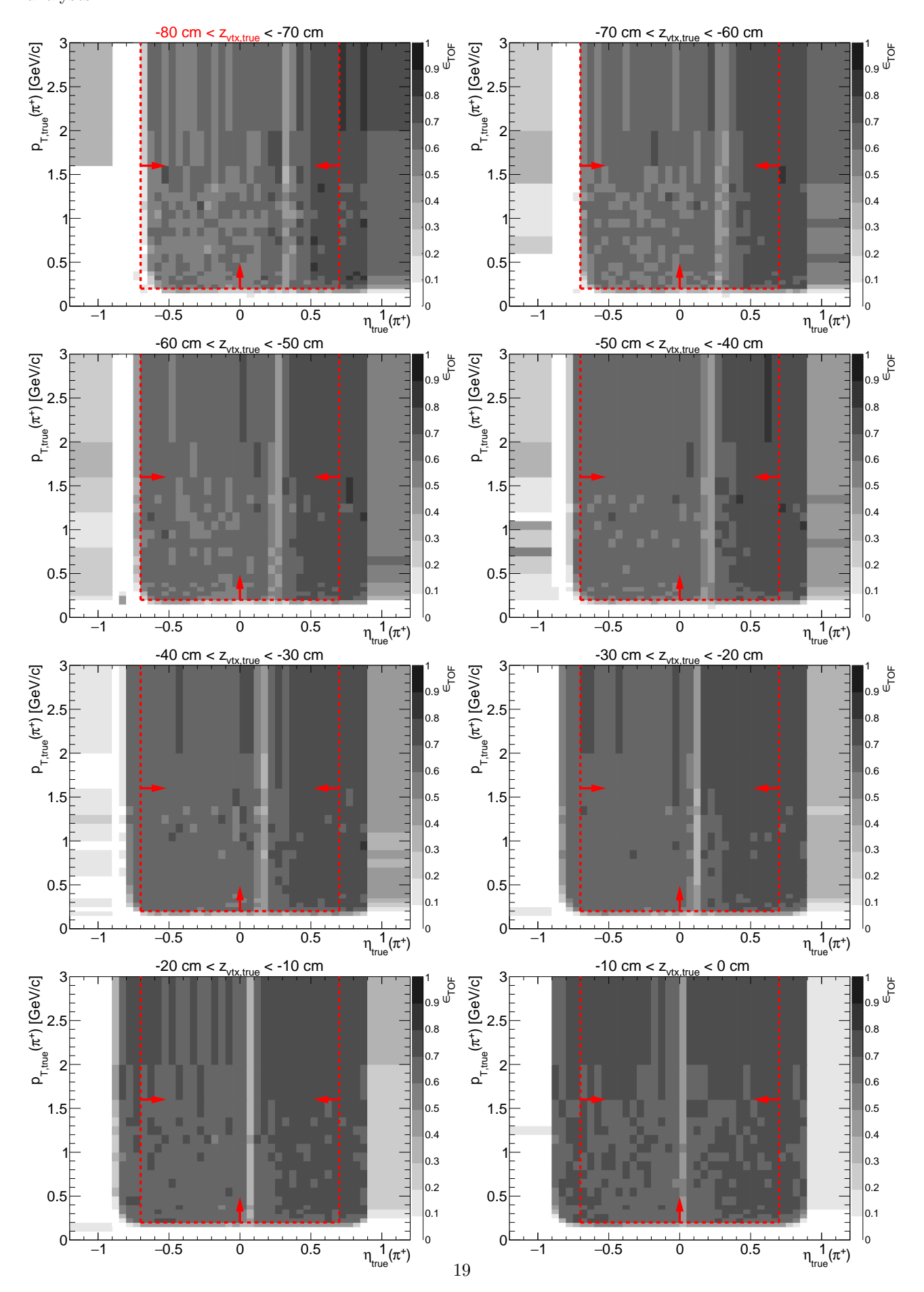


Figure 1.8: TOF acceptance, reconstruction and matching efficiency of π^+ . Each plot represents the TOF efficiency ϵ_{TOF} (z-axis) as a function of true particle pseudorapidity η (x-axis) and transverse momentum p_T (y-axis) in single z-vertex bin whose range is given at the top. Red lines and arrows indicate region accepted in analyses.



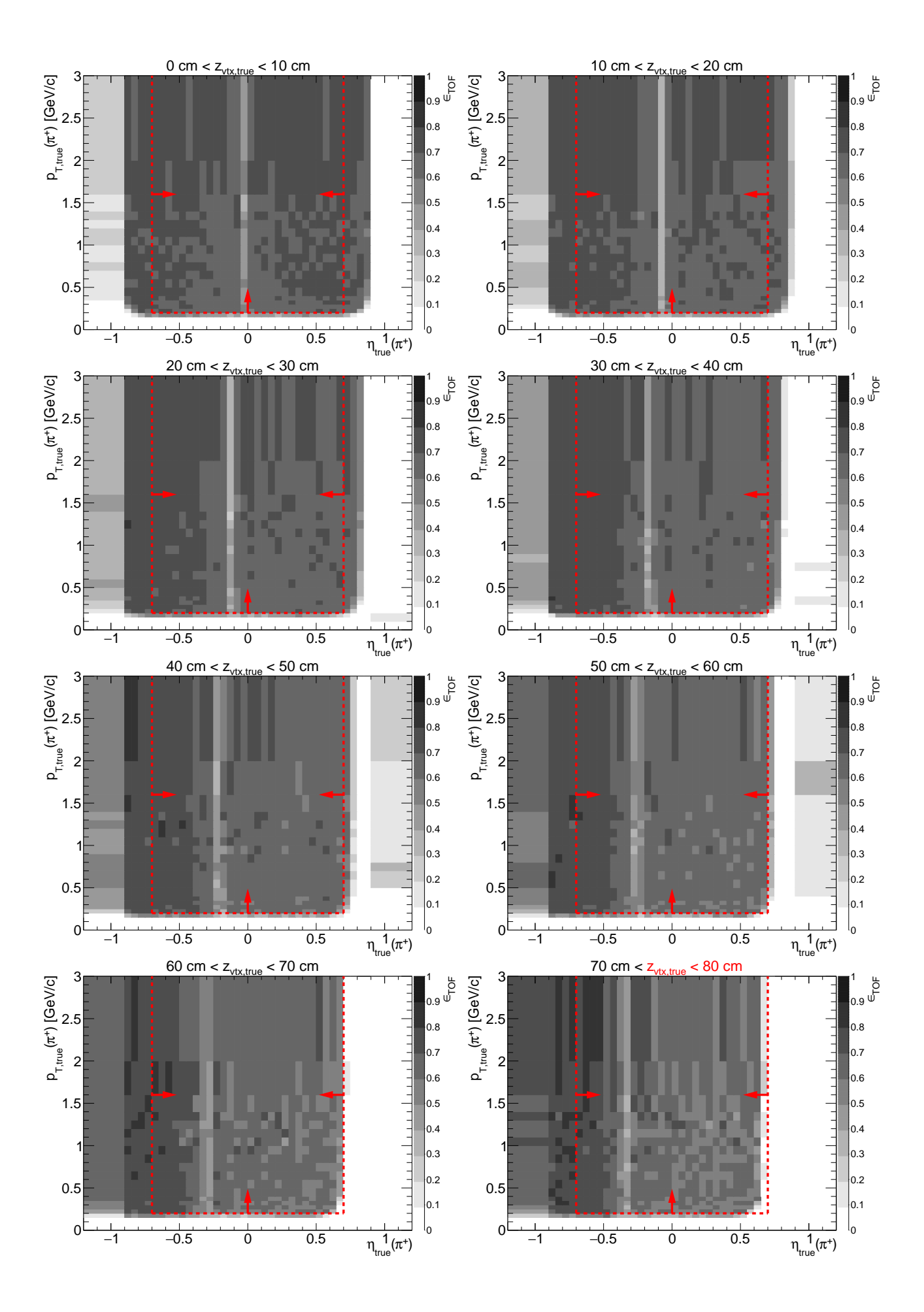
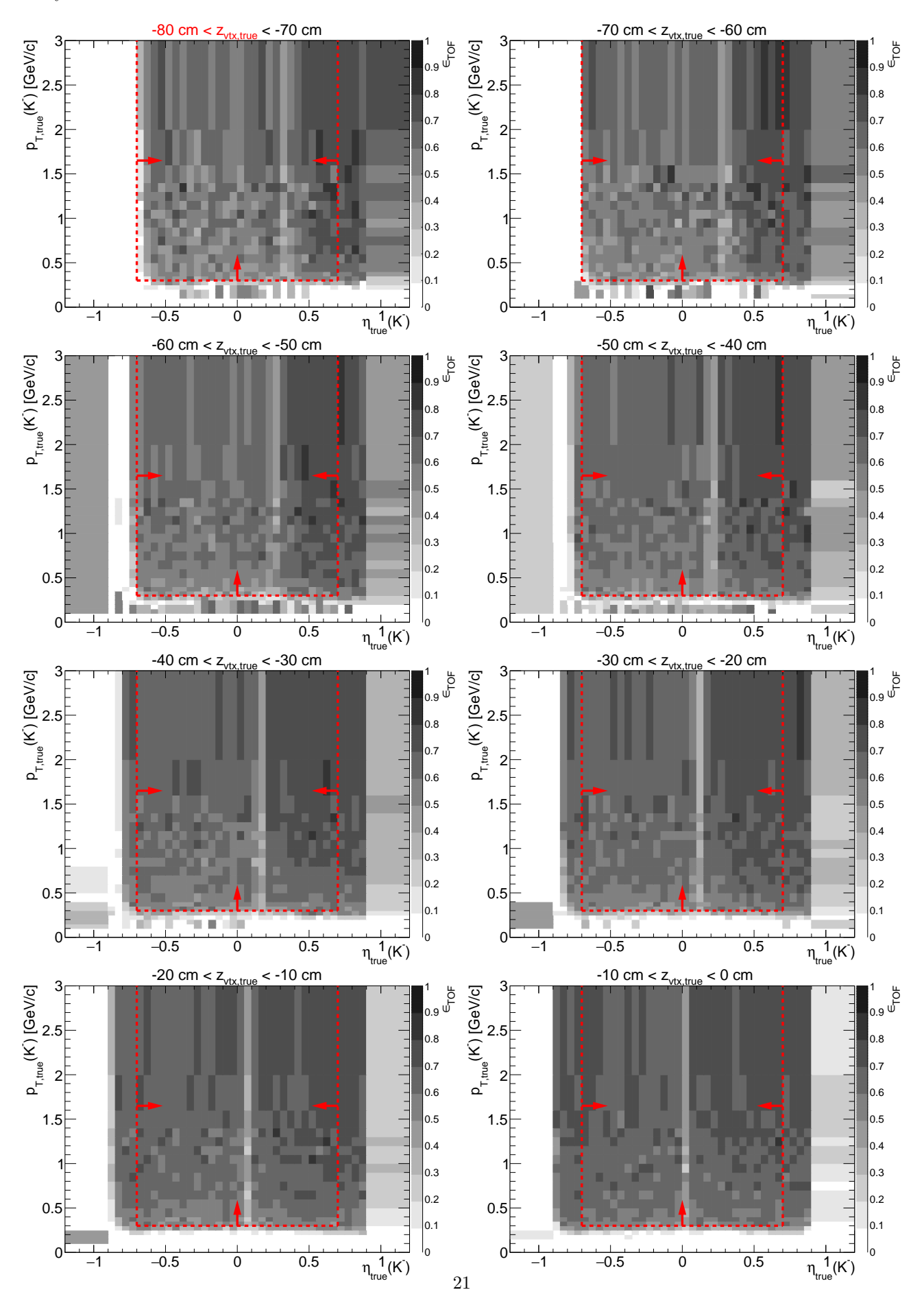


Figure 1.9: TOF acceptance, reconstruction and matching efficiency of K^- . Each plot represents the TOF efficiency ϵ_{TOF} (z-axis) as a function of true particle pseudorapidity η (x-axis) and transverse momentum p_T (y-axis) in single z-vertex bin whose range is given at the top. Red lines and arrows indicate region accepted in analyses.



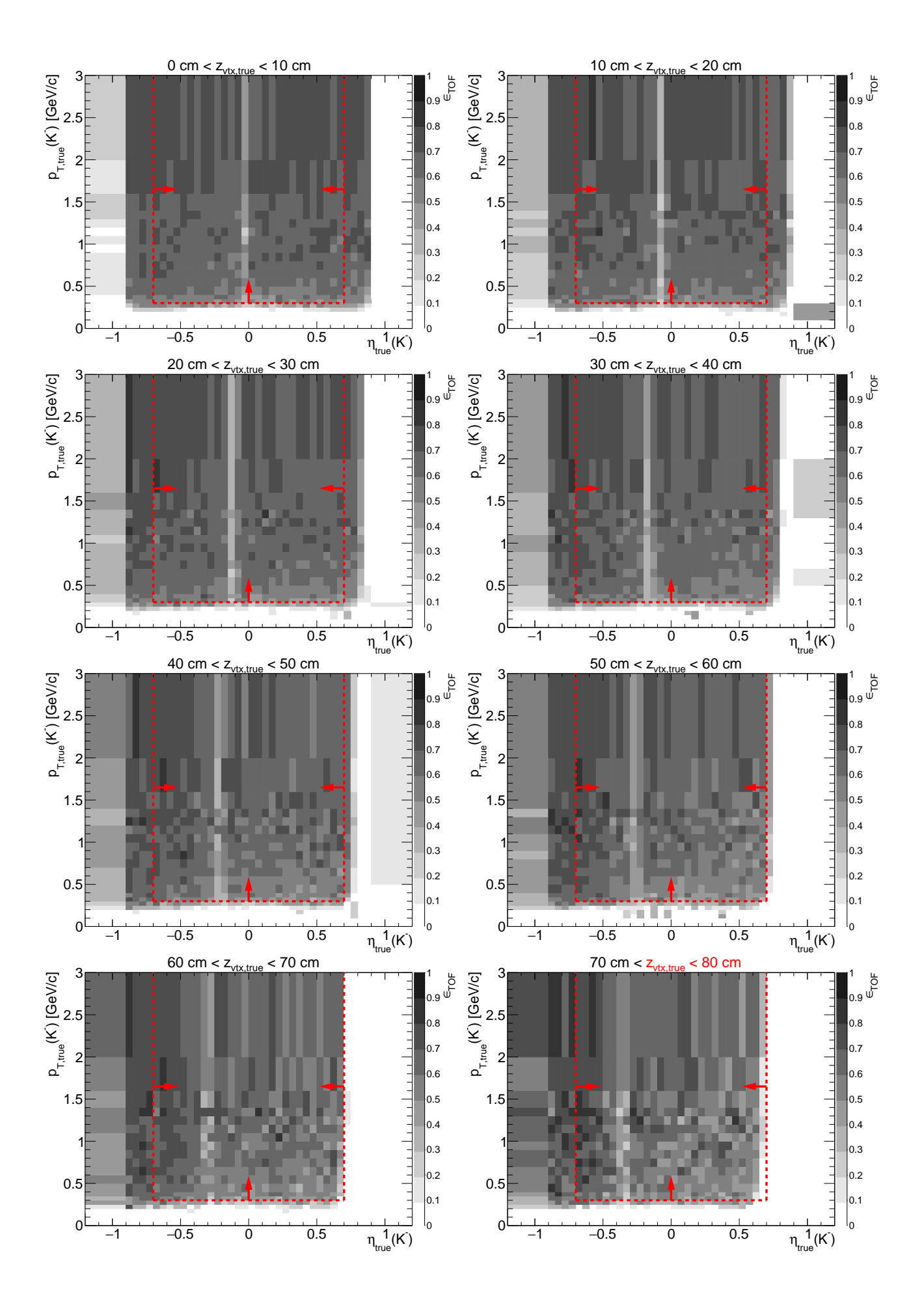
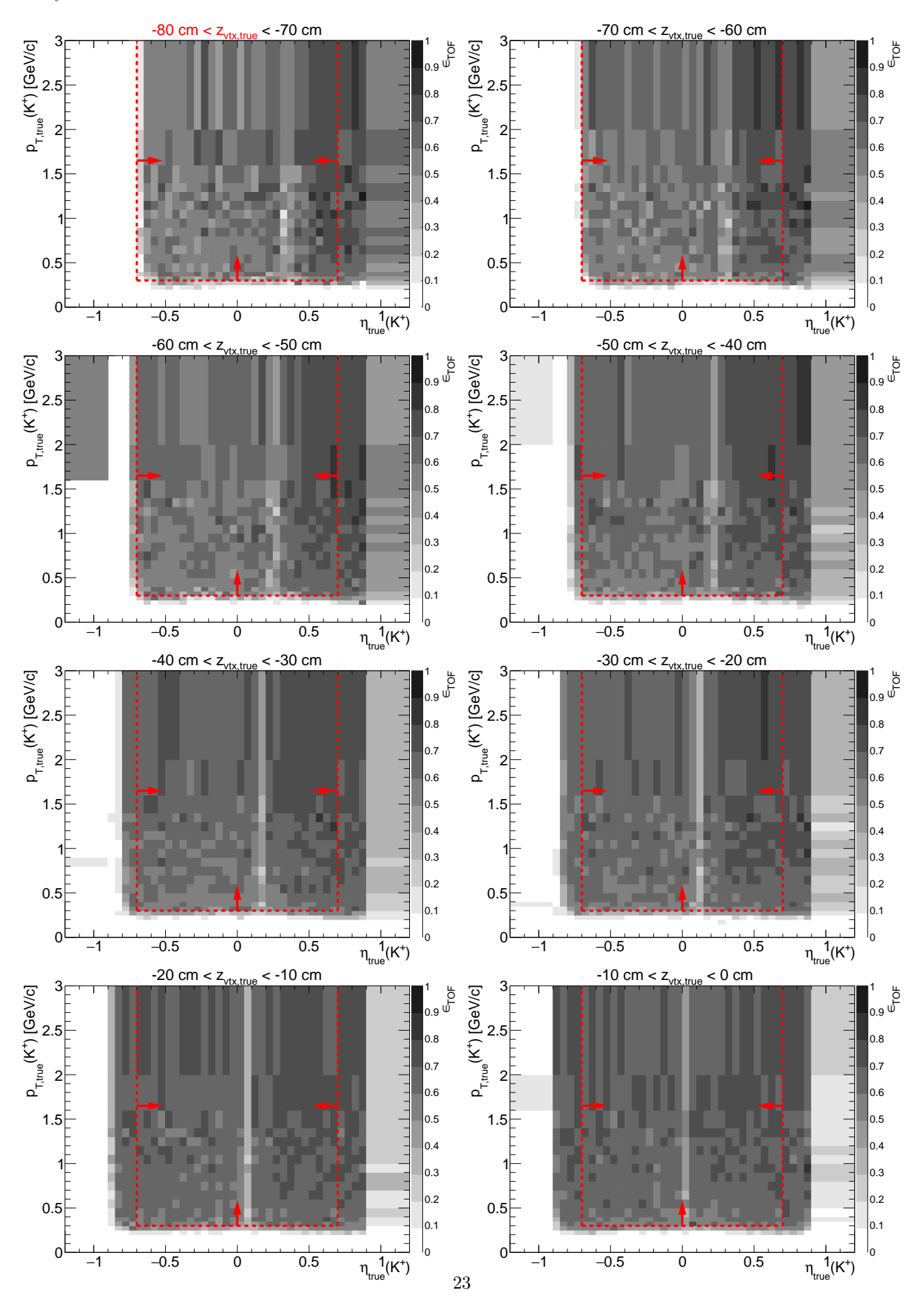


Figure 1.10: TOF acceptance, reconstruction and matching efficiency of K^+ . Each plot represents the TOF efficiency ϵ_{TOF} (z-axis) as a function of true particle pseudorapidity η (x-axis) and transverse momentum p_T (y-axis) in single z-vertex bin whose range is given at the top. Red lines and arrows indicate region accepted in analyses.



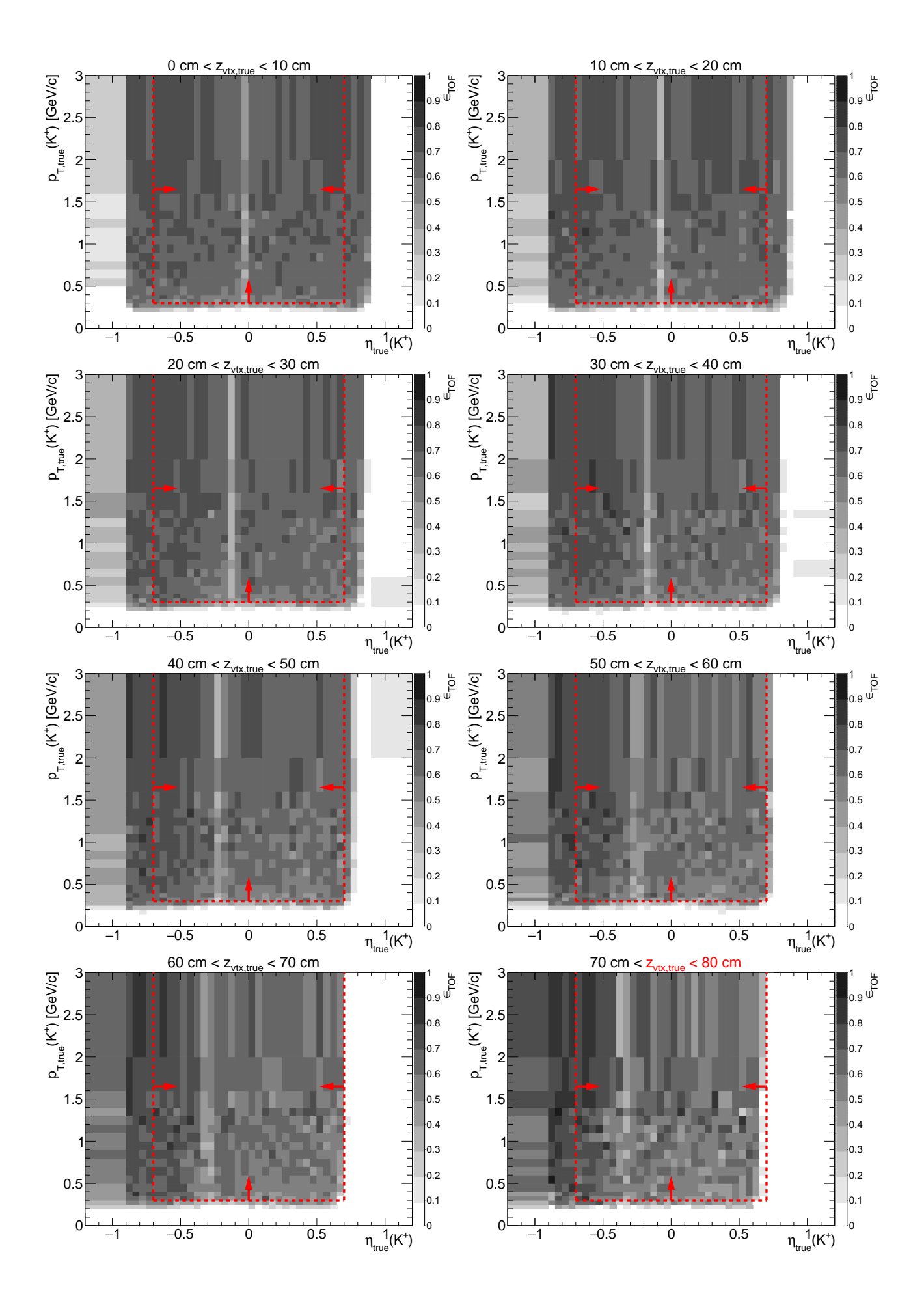
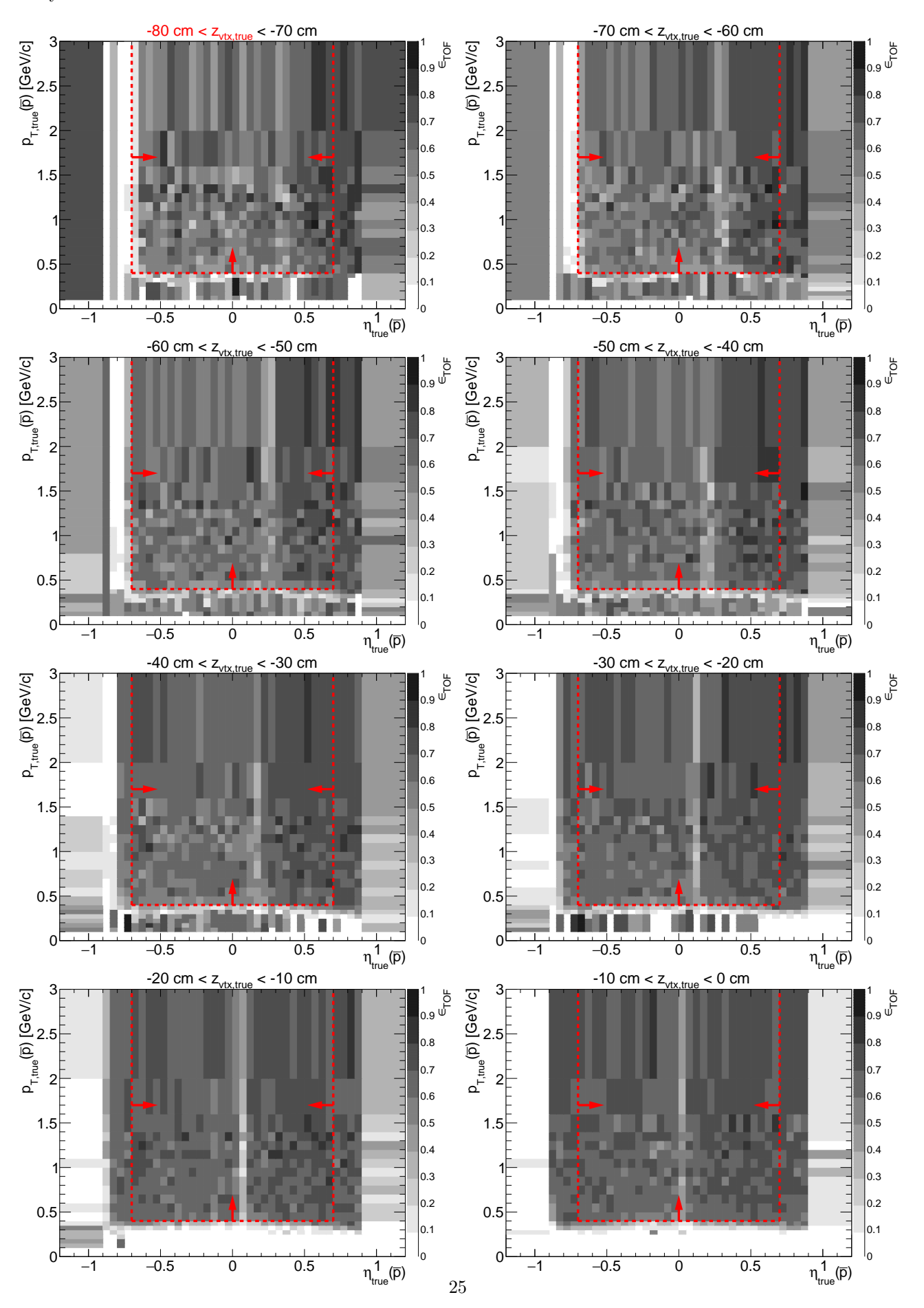


Figure 1.11: TOF acceptance, reconstruction and matching efficiency of \bar{p} . Each plot represents the TOF efficiency ϵ_{TOF} (z-axis) as a function of true particle pseudorapidity η (x-axis) and transverse momentum p_T (y-axis) in single z-vertex bin whose range is given at the top. Red lines and arrows indicate region accepted in analyses.



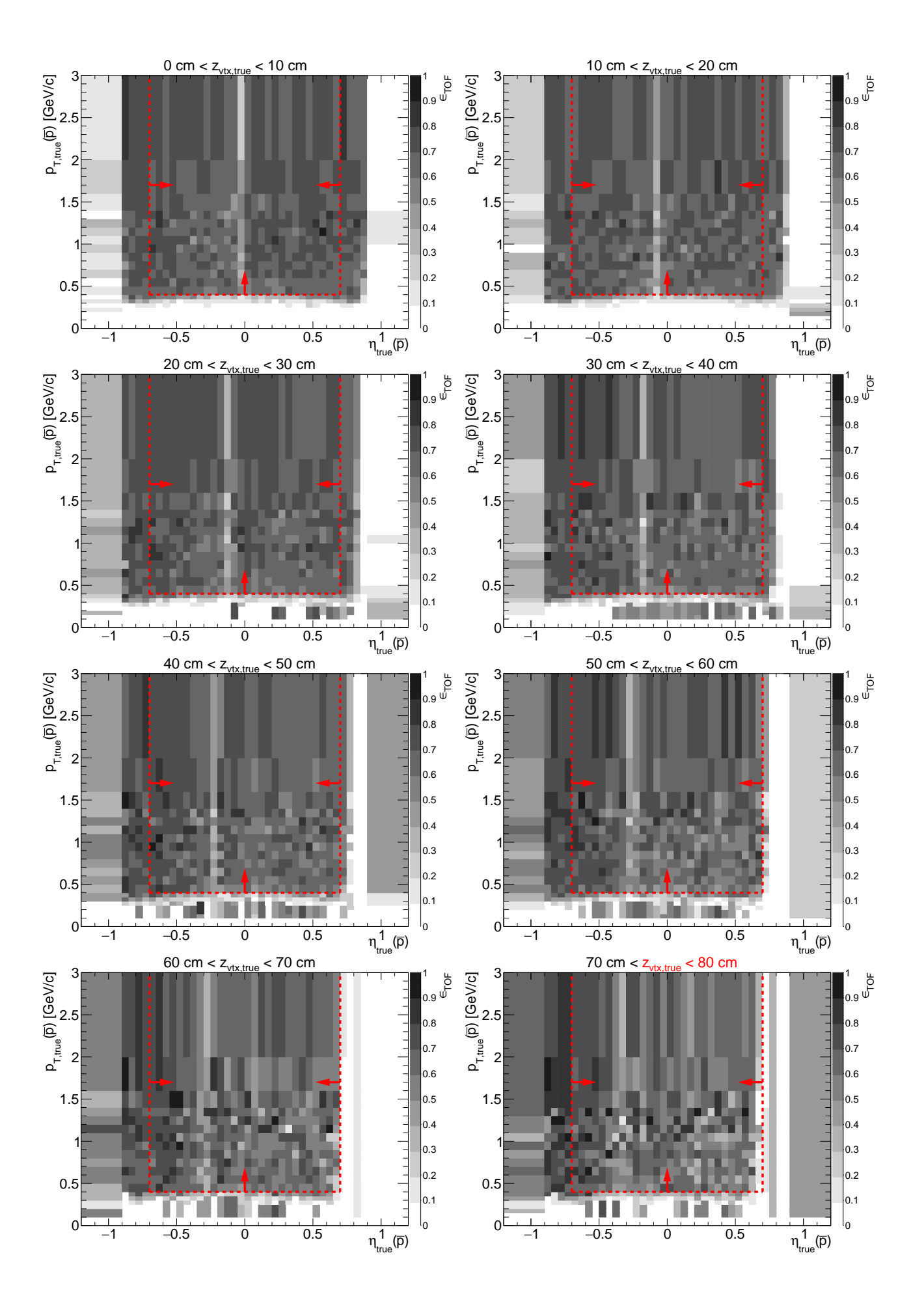
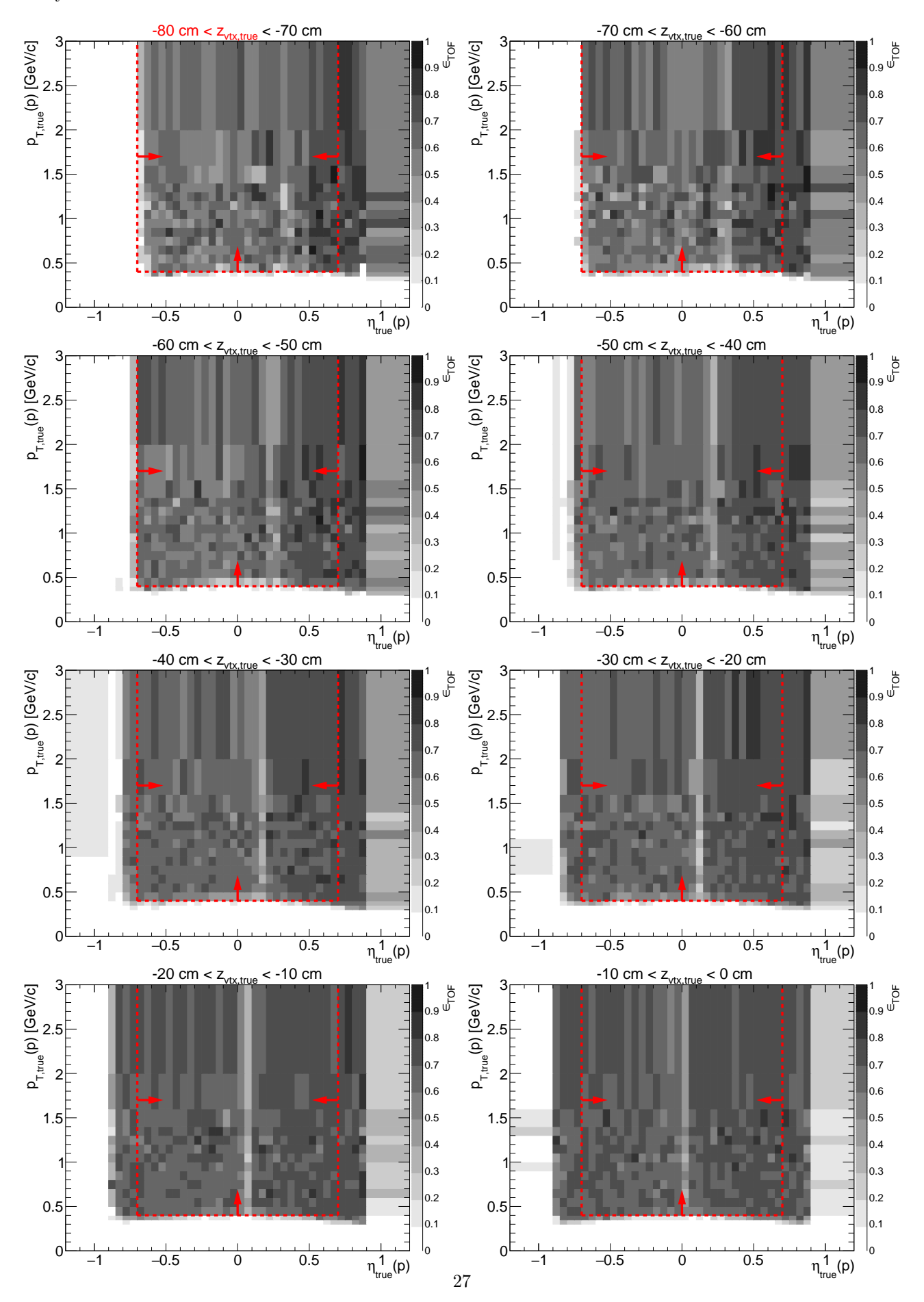
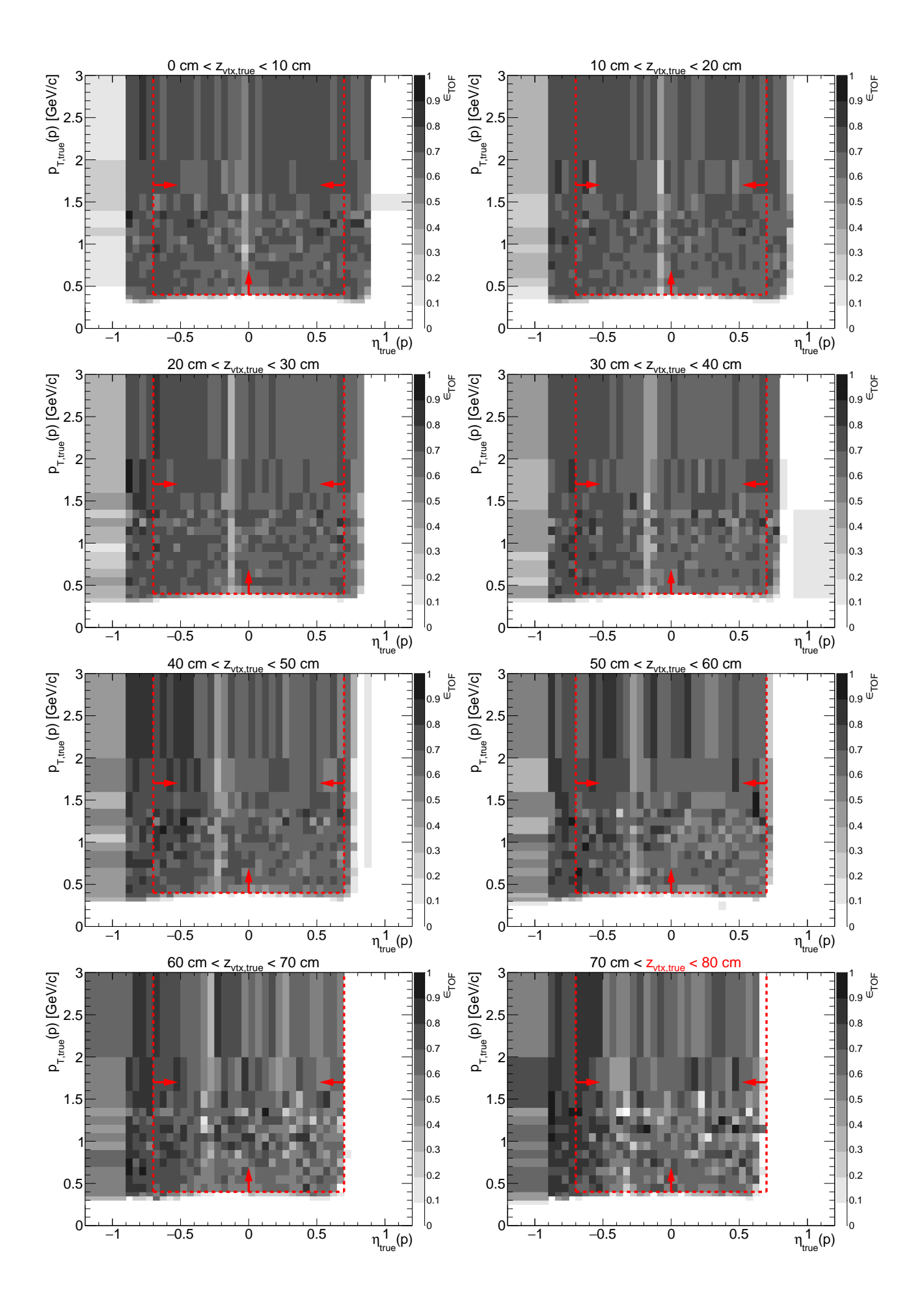


Figure 1.12: TOF acceptance, reconstruction and matching efficiency of p. Each plot represents the TOF efficiency ϵ_{TOF} (z-axis) as a function of true particle pseudorapidity η (x-axis) and transverse momentum p_T (y-axis) in single z-vertex bin whose range is given at the top. Red lines and arrows indicate region accepted in analyses.





1.3 TPC vertex reconstruction efficiency

The definition of vertex reconstruction efficiency established in this analysis is the probability that two global tracks, both associated with true-level primary particles from the kinematic region of the measurement, both satisfying kinematic and quality criteria (cuts ?? and ??) and both matched with hits in TOF, form a vertex listed in the collection of reconstructed primary vertices and DCA(R) and DCA(z) of both global tracks calculated w.r.t. this vertex is contained within the limits of cut ??.

2. Roman Pot simulation

3. dE/dx correction

It is possible to transform dE/dx in MC to make it follow the shape of dE/dx in the data. We know that nSigmaX (where X=Pion, Kaon, Proton, ...) variable follows a gaussian distribution (for particle X)

$$nSigmaX = \left(\ln \frac{dE/dx}{\langle dE/dx \rangle_X}\right)/\sigma_{dE/dx}, \quad f(nSigmaX) = \mathcal{N}(nSigmaX; \mu = 0, \sigma = 1)$$

therefore dE/dx itself follows log-normal distribution:

$$f(dE/dx) = \mathcal{L}og\mathcal{N}(dE/dx; \mu = \langle dE/dx \rangle, \sigma = \sigma_{dE/dx}) = \frac{1}{\sqrt{2\pi} \cdot \sigma \cdot dE/dx} e^{-\frac{\ln^2 \frac{dE/dx}{\langle dE/dx \rangle}}{2\sigma^2}}$$

The transformation we want to apply should preserve the shape of dE/dx (so that it is still described by $\mathcal{L}og\mathcal{N}$), however it should change μ and σ so that these values are eugal to those seen in the data. The transformation that satisfies above postulate is

$$dE/dx' = c \cdot (dE/dx)^a$$

Parameters of the distribution $\mathcal{L}og\mathcal{N}(dE/dx')$ would be then

$$\mu' = c \cdot \mu^a, \quad \sigma' = a \cdot \sigma$$

From above we get formulae for parameters of the transformation:

$$a = \sigma'/\sigma, \quad c = \frac{\mu'}{\mu^a}$$

AlternativeToCrystallBall [3] Eq. (3.1)

$$f(dE/dx) = \begin{cases} \frac{A}{\sqrt{2\pi} \cdot \sigma \cdot dE/dx} \exp\left(-\frac{1}{2} \left(\frac{\ln \frac{dE/dx}{\langle dE/dx \rangle}}{\sigma}\right)^{2}\right) & \text{for } \frac{\ln \frac{dE/dx}{\langle dE/dx \rangle}}{\sigma} \leq k \\ \frac{A}{\sqrt{2\pi} \cdot \sigma \cdot dE/dx} \exp\left(-k \cdot \frac{\ln \frac{dE/dx}{\langle dE/dx \rangle}}{\sigma} + \frac{1}{2}k^{2} - k^{-1} \left(\frac{\ln \frac{dE/dx}{\langle dE/dx \rangle}}{\kappa} - 1\right)^{k}\right) & \text{for } \frac{\ln \frac{dE/dx}{\langle dE/dx \rangle}}{\sigma} > k \end{cases}$$
(3.1)

$$g(p) = P_1 + P_2 \cdot \exp(-P_3 \cdot p) + P_4 \cdot \arctan(P_5 \cdot (p - P_6))$$
(3.2)

PID	$\langle dE/dx angle_{ m Bichsel} - \langle dE/dx angle_{ m MC}$							$\sigma (dE/dx)_{ m MC}$						
1 110	P_1	P_2	P_3	P_4	P_5	P_6	P_1	P_2	P_3	P_4	P_5	P_6		
π^{\pm}	3.618e-8	5.838e-9	5.481				0.0809	-0.023	0.450	-7.84e-3	1.8489	1.04		
K^{\pm}	-1.01e-10	-9.983e-6	7.581				0.0628	0.022	5.381	3.06e-3	7.3070	0.547		
$p,ar{p}$	-4.041e-8	-1.179e-5	4.277				0.0660	0.082	12.042	1.07e-3	7.2872	0.889		
e^{\pm}	-1.542e-7	3.393e-7	5.025				0.0572	0.982	37.984	2.61e-3	-27.995	0.693		
$\overline{d}, \overline{d}$	-2.469e-6	0.3706	21.654	5.131e-7	30.050	0.781	0.1311	-0.971	4.691					

(a)														
PID	$\langle dE/dx angle_{ m Bichsel} - \langle dE/dx angle_{ m Data}$							$\sigma (dE/dx)_{ m Data}$						
	P_1	P_2	P_3	P_4	P_5	P_6	P_1	P_2	P_3	P_4	P_5	P_6		
π^{\pm}	-1.236e-8	1.777e-7	9.938				0.0738	16.86	39.44	-1.704e-3	6.482	0.628		
K^{\pm}	5.49e-10	-2.732e-6	7.712				0.0743	2.67e-5	7.17089					
$p,ar{p}$	-2.140e-7	0.0421	48.305	7.512e-8	15.544	0.575	0.0779	1.822	22.4277					
e^{\pm}	6.701e-8	3.304e-7	7.845				0.0678	468.9	59.4001					
$d, ar{d}$	-1.631e-7	0.0818	18.91				0.1259	-0.288	3.28733					
						(b)								

Table 3.1: Parameters of functions from Fig. 3.2 describing track dE/dx as a function of reconstructed momentum for a few particle species. Units of parameters P_i are such that if one provides momentum in Eq. (3.2) in GeV/c the resultant offset of dE/dx MPV with respect to Bichsel parametrization is in GeV/cm, and the resultant σ parameter is unitless.

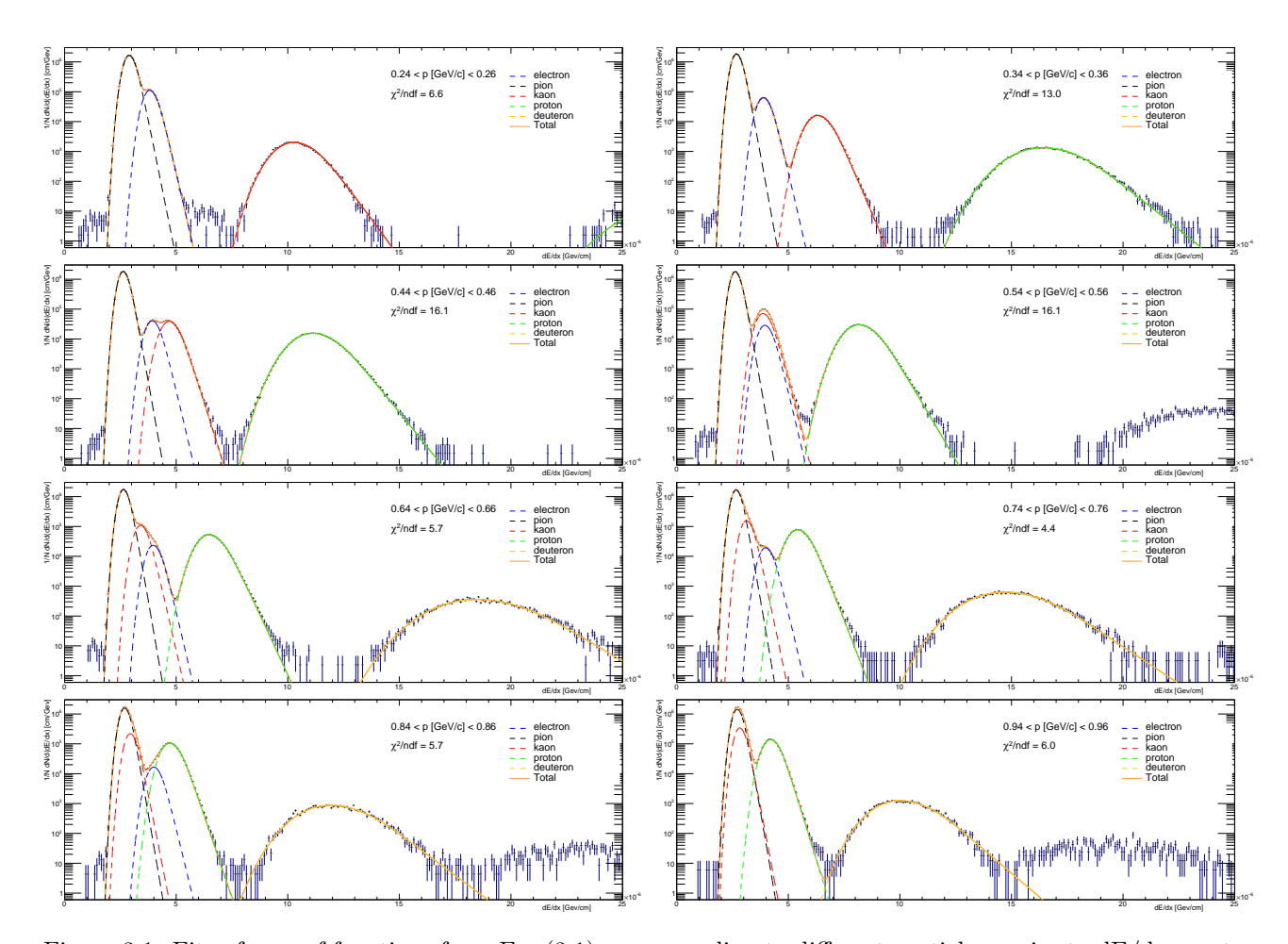


Figure 3.1: Fits of sum of functions from Eq. (3.1) corresponding to different particle species to dE/dx spectra from the data in a few momentum bins.

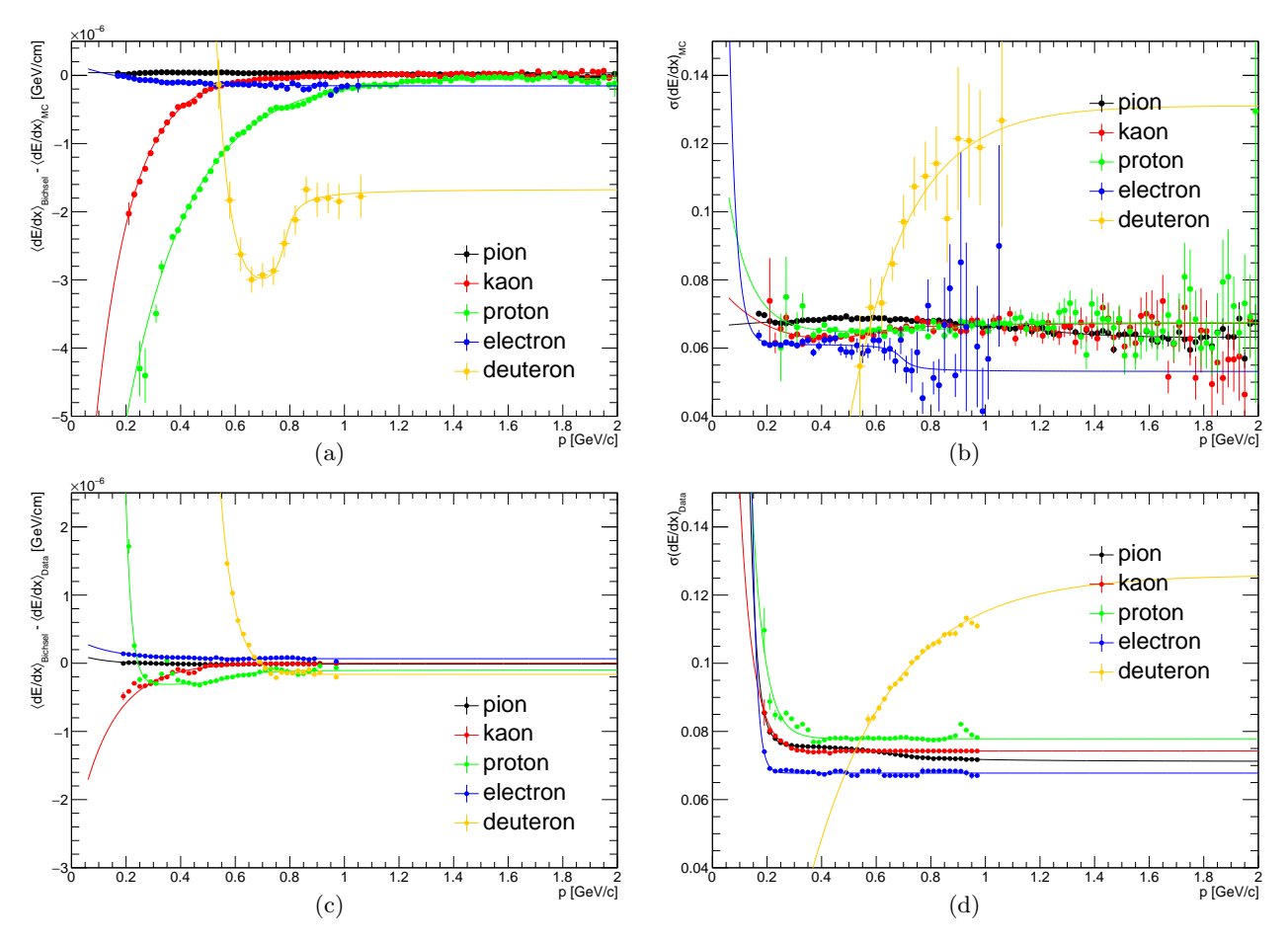


Figure 3.2: Difference between MPV of dE/dx predicted by Bichsel parametrization and obtained from the fit of Eq. (3.1) to dE/dx distribution in the data (3.2c) and MC sample (3.2a) and dE/dx width parameter in data (3.2d) and MC (3.2b) as a function of reconstructed particle momentum for a few particle species. Solid lines represent fits to points of corresponding color.

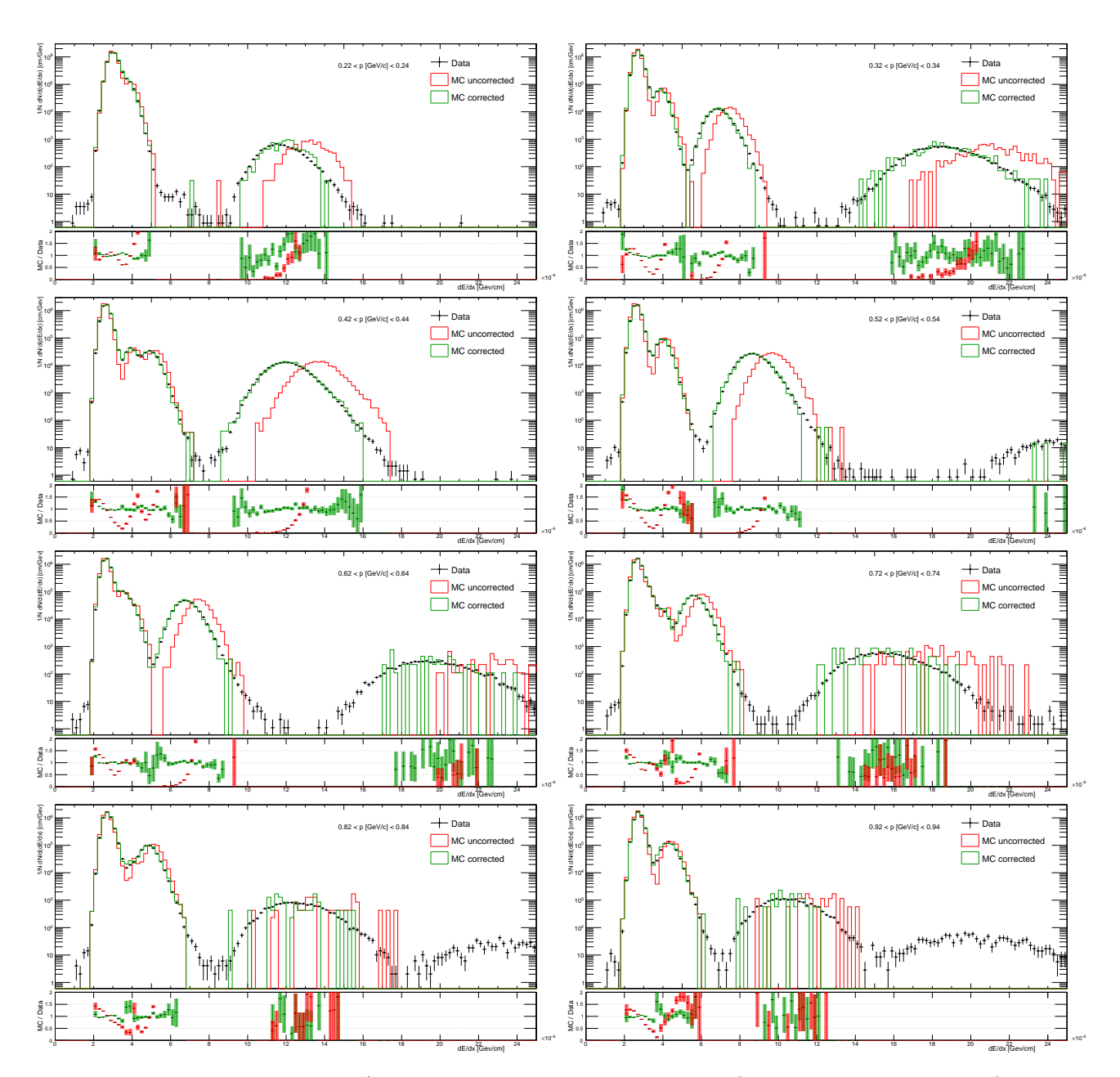


Figure 3.3: Comparison of the dE/dx spectra between the data and MC (before and after correction) in a few momentum bins.

4. TPC track pointing resolution adjustment

It was found during the analysis that distributions of quantities which describe the pointing resolution of the TPC tracks do not agree well between the data and embedded MC. Namely, the resolutions of the global helices associated with the tracks were found to be significantly higher in the STAR simulation than in the data, what manifests as narrower DCA and d_0 distribution in the embedded MC, comparing to corresponding distribution in the data (Fig. 4.5). This issue was discussed under ticket #3332 (Ref. [4]).

This problem could affect the momentum resolution and thus all other resolutions and reponse matrices used in data unfolding. Therefore the resolution adjustment procedure was performed to find appropriate parameters of the "artificial" helix deterioration and finally obtain agreement between DCA and d_0 distributions (and all related resolutions) in the data and embedded MC.

In order to reduce pointing resolution in the MC an additional smearing of the helix radius $\sigma(R)$ was introduced. Based on d_0 comparison in Fig. 4.5a it was decided to account also for the systematic bias of the helix radius $\Delta\mu(R)^1$, which may be present e.g. due to differences in the material budget used the simulation and reconstruction. Both smearing and bias of the helix radius were introduced only for MC tracks which were matched with the true-level particles since only simulated tracks require adjustment (tracks from zero-bias event used in embedding already contain all detector effects).

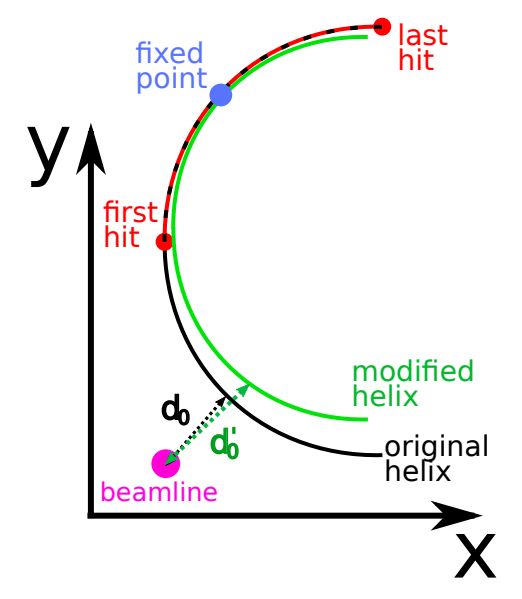


Figure 4.1: Sketch of helix modification procedure and d_0 calculation.

Extraction of $\Delta\mu(R)$ and $\sigma(R)$ parameter required to achieve agreement of pointing resolution between embedded MC and the data involved a few steps, as listed below:

- 1. Series of d_0 histograms in bins of p_T (100 MeV/c wide) was prepared, each for different size of distortion (different $\Delta\mu(R)$ and $\sigma(R)$) of global helix of the TPC tracks matched with true-level particles (example plot in single p_T bin is shown in Fig. 4.2):
 - (a) for each set of parameters $\Delta\mu(R)$ and $\sigma(R)$ the helix radius R was recalculated independently for each track following the Eq. (4.1):

$$R' = R \times \mathcal{N} \Big(1 + \Delta \mu(R), \ \sigma(R) \Big),$$
 (4.1)

(b) new helix of a radius R' was assigned to a track and used to calculate d_0 . The modified helix was obtained by changing the radius of original helix from R to R' with a fixed middle point between the first and last TPC hit of a global track represented by the helix (Fig. 4.1). The momentum of the track was also recalculated:

of the track was also recalculated:
$$p_T' = p_T \times \frac{R'}{R}, \qquad \eta' = \eta \times \frac{R'}{R}. \tag{4.2}$$

- 2. In each p_T bin the χ^2/NDF was calculated between the data and MC d_0 histogram in a range -1.5 cm $< d_0 < 1.5$ cm (corresponding to d_0 cut used in analyses), for every point in parameter space of radius distortion (for every set of $\Delta\mu(R)$ and $\sigma(R)$). An example (single p_T bin) of map of $-\chi^2/\text{NDF}$ in a parameter space is presented in Fig 4.3.
- 3. In each (recalculated) p_T bin the 2-dim parabola $z(x, y; a, b, x_0, y_0, z_0)$ given in Eq. (4.3) ($z = \chi^2/\text{NDF}$, $x = \Delta \mu(R)$, $y = \sigma(R)$) was fitted to $-\chi^2/\text{NDF}$ in the global minimum region to obtain the best-fit distortion parameters. $z = z_0 a(x x_0)^2 b(y y_0)^2. \tag{4.3}$
- 4. The best-fit smearing $\sigma(R)$ (equal to parabola parameter y_0) and best-fit bias $\Delta\mu(R)$ (x_0) from individual p_T bins was plotted as a function of global track p_T (Fig. 4.4). Each point was assigned with an error being a quadratic sum of two components: the error on x_0 (y_0) resulting from the parabola fit to $-\chi^2/\text{NDF}$, and length of corresponding semi-axis of ellipsis formed by the intersection of fitted parabola with the xy-plane at $z=z_0-1/\text{NDF}$ (definition of the parameter uncertainty). Resultant formulae for the error of each individual point in Fig. 4.4 are

¹Transverse impact parameter d_0 takes positive value if the beamline is contained inside the helix (in the yz-plane projection), otherwise it is negative. Any asymmetry in the d_0 distribution in the MC with respect to the data indicates presence of systematic difference in reconstructed d_0 , hence also in reconstructed R.

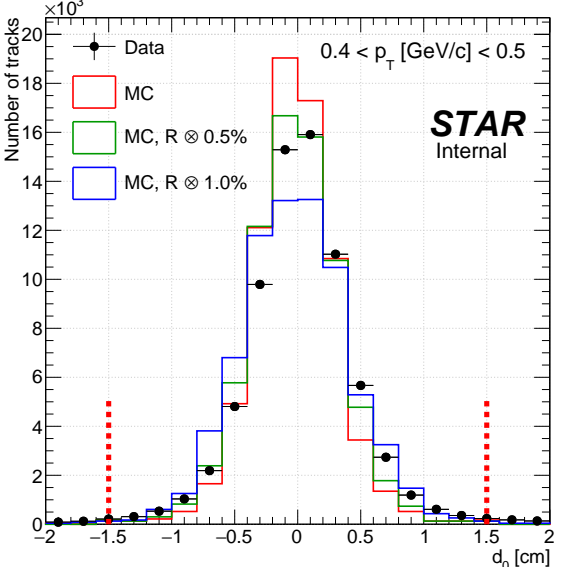


Figure 4.2: Example of comparison of d_0 histograms in single p_T bin in the data (black points) and embedded MC (colored lines) in the procedure of TPC pointing resolution adjustment. MC histograms only for $\Delta\mu(R) = 0$ and $\sigma(R) = 0$, 5×10^{-3} and 10^{-2} were shown for explanatory purposes.

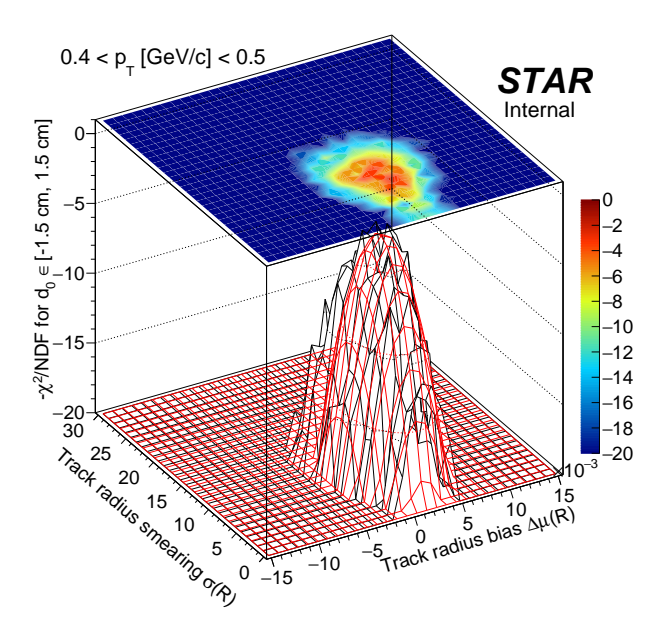


Figure 4.3: Example of $-\chi^2/\text{NDF}$ map in a parameter space in the procedure of TPC pointing resolution adjustment. The red surface represents parabola fitted in the vicinity of the global minimum.

$$\delta\left(\Delta\mu(R)\right) = \sqrt{\delta_{\text{fit}}^2(x_0) + \frac{\text{NDF}}{2a}}, \qquad (4.4) \qquad \qquad \delta\left(\sigma(R)\right) = \sqrt{\delta_{\text{fit}}^2(y_0) + \frac{\text{NDF}}{2b}}. \tag{4.5}$$

From Fig. 4.2 one can read that NDF = 14. In calculation of uncertainties correlation of $\Delta\mu(R)$ and $\sigma(R)$ have not been accounted.

5. The empirically determined functions were fitted to points representing $\Delta \mu(R)$ and $\sigma(R)$ dependence on the global track p_T . Their form and values of parameters are given in Fig. 4.4.

Helices of global TPC tracks were deteriorated according to Eq. (4.1) and the parametrizations of global track p_T -dependence of $\Delta\mu(R)$ and $\sigma(R)$ from Fig. 4.4, to verify if better agreement between the data and embedded MC is found after the adjustment. Filled histograms in Fig. 4.5 show d_0 and DCA distributions after the described adjustment, and filled circles in the bottom pad show their ratio to the data points. Clearly, there is much better agreement between embedded MC and the data after the pointing resolution adjustment. Remaining differences may arise from incomplete theoretical model of the CEP process impleneted in GenEx leading to different p_T spectra of the data and the model (it does not contain resonant $\pi^+\pi^-$ production).

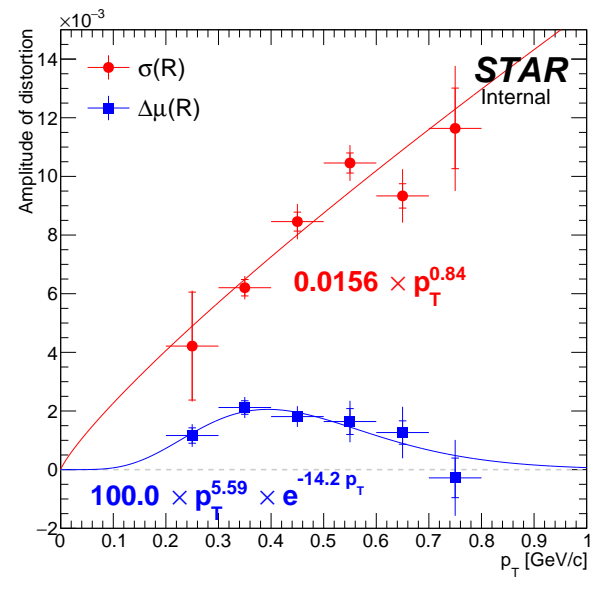
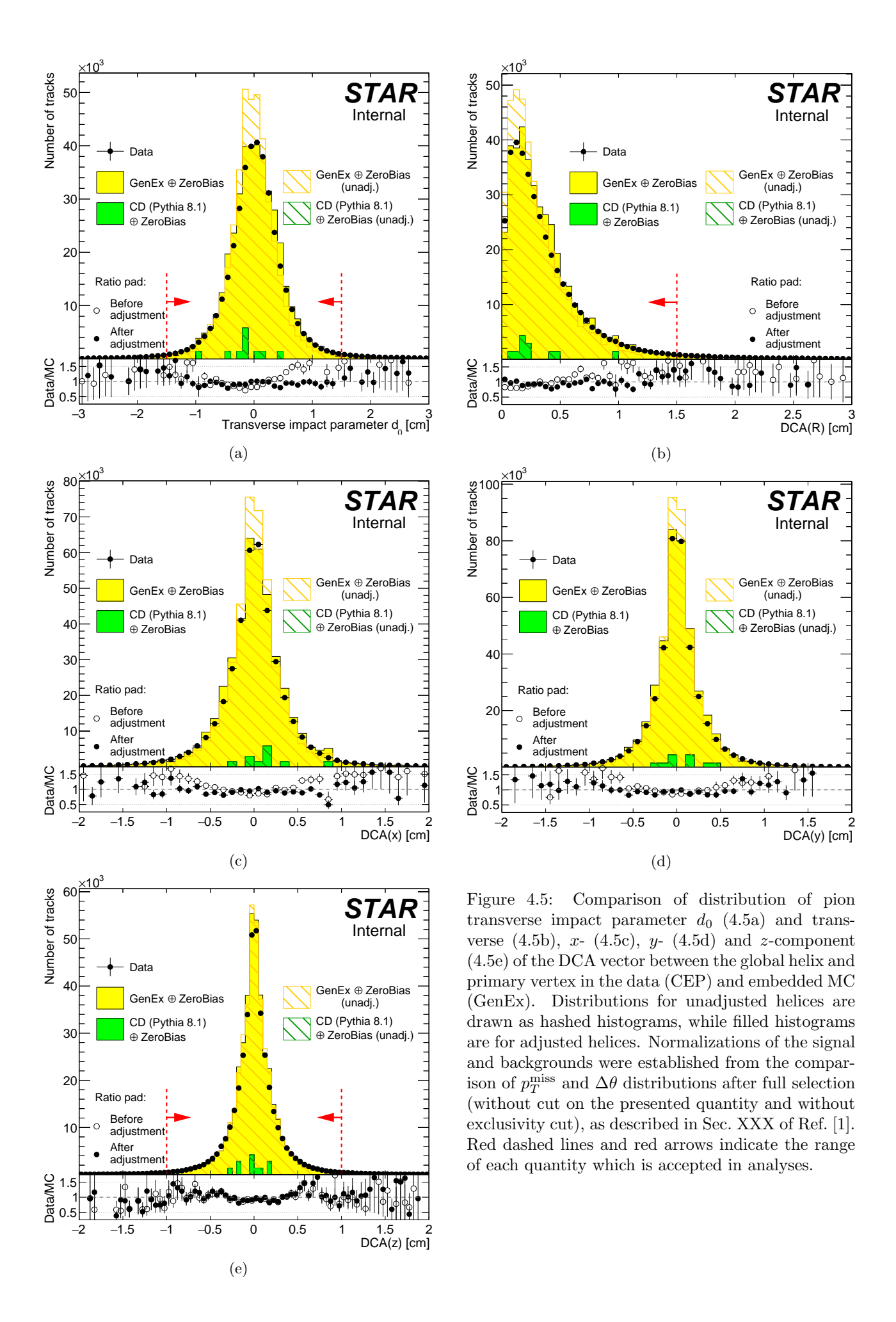


Figure 4.4: Best-fit parameters obtained in the procedure of the TPC track pointing resolution adjustment. Uncertainties on parameters resulting solely from the fit of Eq. (4.3) to $-\chi^2/\text{NDF}$ are represented by the lines with perpendicular endings. Total uncertainties extend beyond. The empirical functions fitted to points are drawn with corresponding colors, and formula of each is written aside.



5. Dead material in front of TPC

6. Systematic errors

List of Figures

1.1	TPC acceptance and reconstruction efficiency of π^-	4
1.2	TPC acceptance and reconstruction efficiency of π^+	6
1.3	TPC acceptance and reconstruction efficiency of K^-	8
1.4		10
1.5		12
1.6		14
1.7	TOF acceptance, reconstruction and matching efficiency of π^-	17
1.8		
1.9	TOF acceptance, reconstruction and matching efficiency of K^-	
	TOF acceptance, reconstruction and matching efficiency of K^+	
	TOF acceptance, reconstruction and matching efficiency of \bar{p}	
1.12	TOF acceptance, reconstruction and matching efficiency of p	27
0.1		20
3.1	Fits to dE/dx spectra from the data	32
3.2	Parameters of track dE/dx as a function of reconstructed momentum for a few particle species	33
3.3	Comparison of dE/dx spectra between data and MC	34
4.1	Sketch of helix modification procedure and d_0 calculation	35
4.1	Example of comparison of d_0 histograms in the data and embedded MC in the procedure of TPC	55
4.2	pointing resolution adjustment	36
4.3	Example of $-\chi^2/\text{NDF}$ map in a parameter space in the procedure of TPC pointing resolution	50
4.5	Example of $-\chi$ /NDF map in a parameter space in the procedure of TTC pointing resolution adjustment	36
4.4	Best-fit parameters obtained in the procedure of the TPC track pointing resolution adjustment.	36
4.4	Comparison of distribution of pion d_0 and components of DCA vector in the data and embedded	50
4.0		37

List of Tables

3.1	Parameters of functions from Fig. 3.2 describing track dE/dx as a function of reconstructed	
	momentum for a few particle species (STARsim MC)	32

References

- $[1] \ \mathtt{https://github.com/rafalsikora/CEP-STAR-AnalysisNote/blob/master/CEP_AnalysisNote.pdf}.$
- [2] http://home.agh.edu.pl/~fulek/PID_AnalysisNote.pdf.
- [3] S. Das, "A simple alternative to the Crystal Ball function," arXiv:1603.08591 [hep-ex].
- $[4] \ \mathtt{https://www.star.bnl.gov/rt3/SelfService/Display.html?id=3332}.$